
Learnable Kernel Density Estimation for Graphs

Xudong Wang¹ Ziheng Sun^{1,2} Chris Ding¹ Jicong Fan^{1,2}

¹School of Data Science, The Chinese University of Hong Kong, Shenzhen (CUHK-Shenzhen), China

²Shenzhen Research Institute of Big Data, Shenzhen, China

{xudongwang, zihengsun}@link.cuhk.edu.cn, {chrisding, fanjicong}@cuhk.edu.cn

Abstract

This work proposes a framework LGKDE that learns kernel density estimation for graphs. The key challenge in graph density estimation lies in effectively capturing both structural patterns and semantic variations while maintaining theoretical guarantees. Combining graph kernels and kernel density estimation (KDE) is a standard approach to graph density estimation, but has unsatisfactory performance due to the handcrafted and fixed features of kernels. Our method LGKDE leverages graph neural networks to represent each graph as a discrete distribution and utilizes maximum mean discrepancy to learn the graph metric for multi-scale KDE, where all parameters are learned by maximizing the density of graphs relative to the density of their well-designed perturbed counterparts. The perturbations are conducted on both node features and graph spectra, which helps better characterize the boundary of normal density regions. Theoretically, we establish consistency and convergence guarantees for LGKDE, including bounds on the mean integrated squared error, robustness, and complexity. We validate LGKDE by demonstrating its effectiveness in recovering the underlying density of synthetic graph distributions and applying it to graph anomaly detection across diverse benchmark datasets. Extensive empirical evaluation shows that LGKDE demonstrates superior performance compared to state-of-the-art baselines on most benchmark datasets.

1 Introduction

Graphs serve as powerful representations for modeling complex relationships and interactions in numerous domains [Wu *et al.*, 2020; Kipf and Welling, 2017; Hamilton *et al.*, 2017; Erica *et al.*, 2020; Nachman and Shih, 2020; Muzio *et al.*, 2020; Rong *et al.*, 2020; Jin *et al.*, 2021b]. The prevalence of graph-structured data has led to significant advances in graph learning, particularly in tasks such as node classification, link prediction, and graph classification [Liu *et al.*, 2023a; Wu *et al.*, 2020]. This rich representation capability makes graphs an essential tool for understanding and analyzing real-world systems ranging from social networks to molecular structures [Wang and Li, 2020; Sun *et al.*, 2019b; Wang *et al.*, 2022].

In this paper, we tackle the fundamental challenge of **modeling the probability density function of graph-structured data**, which serves as a cornerstone for identifying anomalous patterns in graph collections. The significance of this problem spans across numerous real-world applications: from detecting fraudulent communities in social networks [Akoglu *et al.*, 2015; Ding *et al.*, 2019] to identifying rare molecular structures in drug discovery pipelines [Ma *et al.*, 2021; Shen *et al.*, 2024]. Beyond these domains, accurate density estimation of graphs has proven invaluable in biological research, particularly in uncovering novel protein structures that could reveal critical biological mechanisms [Lanciano *et al.*, 2020]. The ubiquity and complexity of these applications underscore the pressing need for effective graph density estimation methods that can capture both structural and semantic patterns while maintaining computational efficiency.

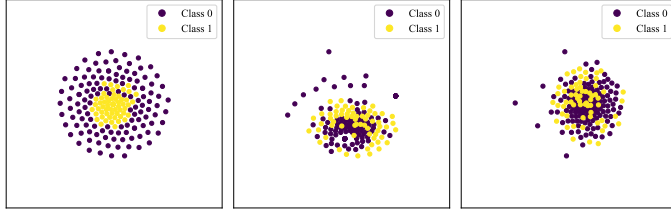


Figure 1: t-SNE visualization (perplexity=30) of learned kernel matrix on MUTAG dataset. Left: LGKDE Learned, Middle: WL Kernel, Right: Propagation Kernel

Traditional approaches to graph density estimation primarily rely on graph kernels combined with kernel density estimation (KDE) [Vishwanathan *et al.*, 2010]. These methods define similarity measures between graphs using various kernels, such as shortest-path kernels [Borgwardt and Kriegel, 2005], Weisfeiler-Lehman subtree (WL) kernels [Shervashidze *et al.*, 2011], and propagation kernel (PK) [Neumann *et al.*, 2016]. However, these approaches face several limitations: i) handcrafted graph kernels may fail to capture complex structural patterns; ii) the computational complexity of kernel computation often scales poorly with graph size; and iii) the fixed bandwidth in traditional KDE may not adapt well to the varying scale of graph patterns.

Figure 1 shows t-SNE [Van der Maaten and Hinton, 2008] visualizations of kernel matrices computed using different methods on the MUTAG dataset. Traditional graph kernels like WL and PK struggle to effectively separate graphs from different classes while our LGKDE learned kernel achieves clear separation between classes while maintaining smooth transitions in the metric space. This comparison underscores the importance of learning adaptive kernel functions that can go beyond purely structural similarities to capture semantic patterns that distinguish functionally different graphs.

More recent methods leverage unsupervised representation learning followed by density estimation. Deep graph neural networks (GNNs) [Kipf and Welling, 2017; Xu *et al.*, 2019] have been employed to learn graph embeddings, which are then used for density estimation or anomaly detection. Several end-to-end approaches have been proposed, such as graph variational autoencoders [Kipf and Welling, 2016], one-class graph neural networks [Zhao and Akoglu, 2021], and contrastive learning-based methods [Qiu *et al.*, 2022; Ma *et al.*, 2022]. However, these methods also have limitations: i) they often make strong assumptions about the shape of the normal data distribution (e.g., hyper-sphere); ii) the learned representations may not preserve important structural information; and iii) the lack of theoretical guarantees makes it difficult to understand their behavior and limitations.

To address the aforementioned challenges, we propose Learnable Kernel Density Estimation for Graphs (LKGDE), a principled framework that bridges deep graph representation learning with adaptive kernel density estimation. LKGDE learns a multi-scale density estimator in a deep Maximum Mean Discrepancy [Gretton *et al.*, 2012] (MMD) based metric space while simultaneously refining graph embeddings through contrastive learning. Our main contributions are as follows:

- We develop a theoretically grounded deep graph MMD model that learns meaningful distances between graphs while preserving the essential properties of MMD.
- We propose a novel multi-scale kernel density estimator with learnable bandwidth weights that dynamically capture both fine-grained local structures and global graph patterns;
- We design an effective structure-aware strategy for generating informative perturbed samples that enable contrastive learning in an unsupervised setting;
- We establish comprehensive theoretical guarantees for our density estimator, including consistency and convergence rates under the graph MMD metric, supported by extensive empirical validation on synthetic graph distribution recovery and superior performance on graph anomaly detection across diverse benchmark datasets.

2 Related Work

This section provides a thorough literature review on density estimation for graphs and graph anomaly detection. The introduction of graph representation learning is presented in Appendix B.1.

2.1 Density Estimation on Graphs

Graph density estimation presents unique challenges due to graph structures' discrete and combinatorial nature. Traditional approaches primarily rely on graph kernels [Vishwanathan *et al.*, 2010], which define similarity measures between graphs through various structural features. Representative examples include the random walk kernel [Kashima *et al.*, 2003], shortest-path kernel [Borgwardt and Kriegel, 2005], and Weisfeiler-Lehman subtree kernel [Shervashidze *et al.*, 2011]. These kernels or the embeddings computed from the kernel matrices, combined with kernel density estimation (KDE), provide a principled way to model graph distributions. However, they face several limitations: i) the fixed kernel design may not capture complex structural patterns; ii) the computational complexity typically scales poorly with graph size; and iii) the bandwidth selection in KDE remains challenging for graph-structured data.

Recent advances in deep learning have inspired new approaches to graph density estimation. Graph variational autoencoders [Kipf and Welling, 2016] attempt to learn a continuous latent space where density estimation becomes more tractable. Flow-based models [Liu *et al.*, 2019] and energy-based models [Liu *et al.*, 2020] offer alternative frameworks for modeling graph distributions. However, these methods often make strong assumptions about the underlying distribution or struggle with the discrete nature of graphs. Moreover, the lack of theoretical guarantees makes it difficult to understand their behavior and limitations, particularly in the context of anomaly or outlier detection [Pang *et al.*, 2021; Jin *et al.*, 2021a; Liu *et al.*, 2023b; Cai *et al.*, 2024].

2.2 Graph Anomaly Detection

Graph anomaly detection has attracted significant attention due to its broad applications in network security, fraud detection, and molecular property prediction [Akoglu *et al.*, 2015; Ma *et al.*, 2021]. Early approaches primarily focus on node or edge-level anomalies within a single graph [Ding *et al.*, 2019], while graph-level anomaly detection presents distinct challenges in characterizing the normality of entire graph structures [Zhao and Akoglu, 2021]. Recent studies have further expanded this field into graph-level out-of-distribution (OOD) detection, which aims to identify whether a test graph comes from a different distribution than the training data [Liu *et al.*, 2023a].

Recent developments in deep learning have led to several innovative approaches. One prominent direction adapts deep one-class classification frameworks to graphs. For instance, OCGIN [Zhao and Akoglu, 2021] combines Graph Isomorphism Networks with deep SVDD to learn a hyperspherical decision boundary in the embedding space. OCGTL [Qiu *et al.*, 2022] further enhances this approach through neural transformation learning to address the performance flip issue. Another line of research leverages reconstruction-based methods, where graph variational autoencoders [Kipf and Welling, 2016] or adversarial architectures are employed to learn normal graph patterns.

Knowledge distillation and contrastive learning have emerged as powerful tools for graph anomaly detection. GLocalKD [Ma *et al.*, 2022] distills knowledge from both global and local perspectives to capture comprehensive normal patterns. Recent works like iGAD [Zhang *et al.*, 2022] propose dual-discriminative approaches combining attribute and structural information, while CVTGAD [Li *et al.*, 2023] employs cross-view training for more robust detection. SIGNET [Liu *et al.*, 2023b] proposes a self-interpretable approach by introducing a multi-view subgraph information bottleneck for detecting anomalies. In the realm of graph OOD detection, methods such as GOOD-D [Liu *et al.*, 2023a] and GraphDE [Li *et al.*, 2022] have been developed to handle distribution shifts in graph data, demonstrating the close connection between anomaly detection and OOD detection tasks.

Despite the advances, existing methods face limitations: i) strong assumptions about the distribution of normal graphs (e.g., hyperspherical or Gaussian); ii) limited theoretical understanding of their behavior; iii) challenges in handling the heterogeneity and non-IID nature of graph data distributions [Kairouz *et al.*, 2021; Xie *et al.*, 2021; Cai *et al.*, 2024].

3 Methodology

3.1 Problem Definition

Consider a collection of normal graphs $\mathcal{G} = \{G_1, \dots, G_N\}$, where each graph $G_i = (V_i, E_i, \mathbf{X}_i)$ consists of a node set V_i , an edge set E_i , and node features $\mathbf{X}_i \in \mathbb{R}^{|V_i| \times d}$. We denote the adjacency

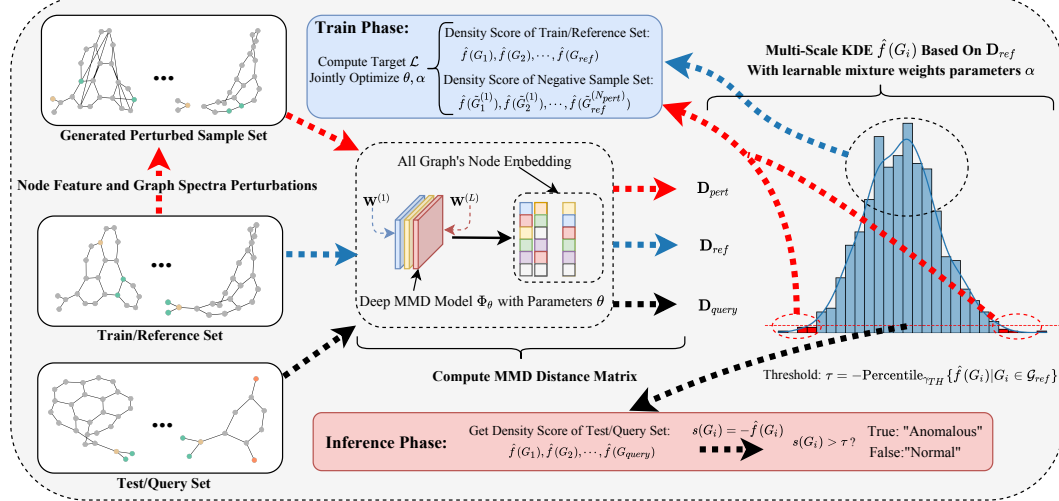


Figure 2: Framework of our proposed LGKDE

matrix of G_i as \mathbf{A}_i . Our goal is to learn a density estimator $f : \mathbb{G} \rightarrow \mathbb{R}_+$ that maps graphs to non-negative density values, capturing the underlying distribution of \mathcal{G} . Note that \mathbb{G} denotes the set of all graphs in the form of $G = (V, E, \mathbf{X})$, where the \mathbf{X} are drawn from some continuous distribution.

The key technical challenges stem from several unique characteristics of graph data:

- **Distribution Complexity:** Graph-structured data exhibits complex patterns at multiple scales and can undergo various types of distributional shifts. These include structural variations (from local substructures to global topological properties), size shifts (varying numbers of nodes and edges), and feature shifts (changes in node attributes), requiring robust and adaptive modeling approaches.
- **Isomorphism Invariance:** The density estimator must be invariant to node permutations while remaining sensitive to structural differences that indicate anomalies.
- **Limited Supervision:** The unsupervised nature of the problem requires learning meaningful representations and density estimates without access to labeled anomalies.

These challenges motivate our development of LGKDE, a learnable kernel density estimation framework that can effectively model distributions of graph-structured data through deep learning methods.

3.2 Overview of LGKDE Framework

At a high level, our LGKDE framework aims to learn a density estimator for graph-structured data by combining the expressiveness of deep learning the well-established kernel density estimation approach. The key insight is to construct a learnable metric space using MMD where we can effectively estimate graph densities while maintaining theoretical guarantees. Formally, our framework consists of three main components (Figure 2 and Algorithm 3): (1) a deep graph MMD model that learns meaningful distances between graphs; (2) a multi-scale kernel density estimator with learnable weights that adaptively captures density patterns at different scales; and (3) a structure-aware sample generation mechanism that enables contrastive learning to refine the learned representations and decision boundaries. The whole method is formulated as

$$\max_{\theta} \sum_{i=1}^N \sum_{j=1}^{N_{\text{pert}}} \frac{p_{\theta}(G_i) - p_{\theta}(\tilde{G}_i^{(j)})}{p_{\theta}(G_i)} \quad (1)$$

where $p_{\theta}(G)$ denotes the probability density of a graph G , θ denotes the parameters to learn in our LGKDE model, and $\tilde{G}_i^{(j)}$ denotes the j th perturbed counterpart of G_i . More details about the motivation and rationale of (1) will be provided in the following sections.

3.3 Graph Maximum Mean Discrepancy

Inspired by [Sun and Fan, 2024], we use a deep graph MMD model to compute meaningful distances between graphs. The key idea is to represent each graph as a distribution over its node embeddings and measure graph similarity through MMD [Gretton *et al.*, 2012].

Specifically, given a graph $G_i = (V_i, E_i, \mathbf{X}_i)$ with adjacency matrix \mathbf{A}_i and node feature matrix \mathbf{X}_i , we learn node embeddings via a GNN with parameters θ :

$$\mathbf{Z}_i = \text{GNN}_\theta(\mathbf{A}_i, \mathbf{X}_i) \quad (2)$$

where $\mathbf{Z}_i \in \mathbb{R}^{n_i \times d_{\text{out}}}$, $n_i = |V_i|$, and each row of \mathbf{Z}_i is the d_{out} -dimension embedding of a node on G_i . Let $\mathbf{z}_p^{(i)}$ is the p -th row of \mathbf{Z}_i , the deep MMD distance between graphs [Sun and Fan, 2024] is

$$d_{\text{MMD}}(G_i, G_j) = \sup_{k_\gamma^{\text{emb}} \in \mathcal{K}_{\text{emb}}} \left(\frac{1}{n_i^2} \sum_{p,q=1}^{n_i, n_i} k_\gamma^{\text{emb}}(\mathbf{z}_p^{(i)}, \mathbf{z}_q^{(i)}) + \frac{1}{n_j^2} \sum_{p,q=1}^{n_j, n_j} k_\gamma^{\text{emb}}(\mathbf{z}_p^{(j)}, \mathbf{z}_q^{(j)}) - \frac{2}{n_i n_j} \sum_{p=1}^{n_i} \sum_{q=1}^{n_j} k_\gamma^{\text{emb}}(\mathbf{z}_p^{(i)}, \mathbf{z}_q^{(j)}) \right)^{1/2} \quad (3)$$

where \mathcal{K}_{emb} is a family of characteristic kernels (e.g., Gaussian function) and each instance $k_\gamma^{\text{emb}}(\cdot, \cdot)$ uses a hyperparameter $\gamma \in \Gamma_{\text{emb}} := \{\gamma_1, \dots, \gamma_S\}$. For a Gaussian family, $k_\gamma^{\text{emb}}(\mathbf{u}, \mathbf{v}) = \exp(-\gamma_s \|\mathbf{u} - \mathbf{v}\|^2)$. Intuitively, for each γ , we compare the distributions of node embeddings in G_i and G_j . And the MMD distance takes the supremum over all kernels in \mathcal{K}_{emb} to capture multi-scale structure.

In our proposed LGKDE, we develop a deep graph MMD model, a L -layer GNN as our graph encoder Φ_θ with parameters $\theta = \{\mathbf{W}^{(l)} \in \mathbb{R}^{d_{l-1} \times d_l}\}_{l=1}^L$ and ReLU activation function to learn node embeddings for the deep MMD metric computation. The whole computation pseudocode through the deep MMD model is shown in Algorithm 2.

This deep graph MMD model serves three crucial purposes: (1) learning structure-aware graph representations; (2) providing a theoretically grounded metric space for density estimation; and (3) enabling end-to-end learning through its fully differentiable architecture.

3.4 Learning Graph Density Estimation

Based on the learned MMD metric space, we propose a learnable density estimation framework that combines structured graph perturbations with adaptive kernel density estimation. Our framework learns all parameters by maximizing the density of normal graphs relative to their perturbed counterparts, enabling effective capture of both structural and semantic patterns.

3.4.1 Structure-aware Sample Generation

To enhance the learning of the density estimator without requiring labeled anomalies, we introduce a structure-aware sample generation mechanism. The key idea is to create perturbed versions of normal graphs that preserve essential structural properties while introducing controlled variations. For each normal graph G , we generate perturbed samples through two types of perturbations:

1) Node Feature Perturbation: We randomly modify the features of a subset of nodes while preserving the graph structure:

$$\mathbf{X}'_v = \begin{cases} \mathbf{X}_{\text{perm}(v)} & \text{if } v \in \mathcal{V}_{\text{swap}} \\ \mathbf{X}_v & \text{otherwise} \end{cases} \quad (4)$$

where $\text{perm}(v)$ is a random permutation and $\mathcal{V}_{\text{swap}}$ contains $r_{\text{swap}}|V|$ randomly selected nodes.

2) Energy-based Spectral Perturbation: Given an adjacency matrix \mathbf{A} , we perform SVD decomposition $\mathbf{A} = \mathbf{U}\Sigma\mathbf{V}^T$. Let $\sigma_i|_{i=1}^n$ be the singular values in descending order. We define the cumulative energy ratio up to index k as:

$$E(k) = \frac{\sum_{i=1}^k \sigma_i^2}{\sum_{i=1}^n \sigma_i^2} \quad (5)$$

Using energy thresholds $\tau_1 = 0.5$ and $\tau_2 = 0.75$, we partition the singular values into three groups:

$$\mathcal{S}_h = \{\sigma_i : E(i) \leq \tau_1\} \quad \mathcal{S}_m = \{\sigma_i : \tau_1 < E(i) \leq \tau_2\} \quad \mathcal{S}_l = \{\sigma_i : E(i) > \tau_2\}$$

So we can decide the fraction p_{pert} of total singular values to be modified. We compute an adaptive ratio $r = \min(\mu_h/\mu_l, r_{\text{max}})$, where μ_h and μ_l are the means of \mathcal{S}_h and \mathcal{S}_l respectively, and $r_{\text{max}} =$

10. For edge addition/removal (operation $flag \in \{1, 0\}$), we modify the singular values as:

$$\tilde{\sigma}_i = \begin{cases} \sigma_i/r & \text{if } \sigma_i \in \mathcal{S}_h \text{ and } flag = 0 \quad (\text{edges removal}) \\ r\sigma_i & \text{if } \sigma_i \in \mathcal{S}_l \text{ and } flag = 1 \quad (\text{edges addition}) \\ \sigma_i & \text{otherwise} \end{cases} \quad (6)$$

The perturbed adjacency matrix is reconstructed as $\tilde{\mathbf{A}} = \mathbf{U}\tilde{\Sigma}\mathbf{V}^T$ (with the fraction p_{pert} of total singular values is modified). As shown in Figure 3, this generates structurally meaningful variations while preserving the graph’s core topology. Algorithm 1 shows the pseudocode.

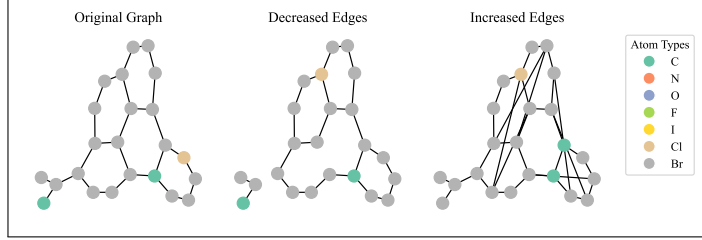


Figure 3: Demonstration of the node feature and energy-based spectral perturbation on a MUTAG molecule. Left: original graph; Middle: edge removal through high-energy group division; Right: edge addition through low-energy group multiplication. See more case studies in Appendix C.

3.4.2 Density Learning Framework

We design an adaptive density estimation framework that jointly learns kernel parameters and density estimates through contrastive optimization. For a graph G in our reference set $\mathcal{G} = \{G_1, \dots, G_N\}$, we define its density using a multi-scale kernel density estimator:

$$\hat{f}_{KDE}(G) = \sum_{k=1}^M \pi_k(\boldsymbol{\alpha}) \phi_k(G), \quad \pi_k(\boldsymbol{\alpha}) = \frac{\exp(\alpha_k)}{\sum_{l=1}^M \exp(\alpha_l)} \quad (7)$$

where each component density $\phi_k(G)$ represents a kernel density estimate at bandwidth $h_k \in H_{KDE}$, and $\pi_k(\boldsymbol{\alpha})$ are learnable mixture weights parameterized by $\boldsymbol{\alpha}$ through a softmax function. Each component density is computed as:

$$\phi_k(G) = \frac{1}{N} \sum_{i=1}^N K_{KDE}(d_{MMD}(G, G_i), h_k), \quad h_k \in H_{KDE} \quad (8)$$

where $K_{KDE}(d, h) = \frac{1}{C_{d_{\text{int}}} h^{d_{\text{int}}}} K_0\left(\frac{d^2}{h^2}\right)$ is a kernel function with bandwidth h and kernel profile K_0 and d_{int} is the intrinsic dimension of the space induced by the input distance metric d . For a Gaussian kernel profile, $K_0(t) = e^{-t/2}$ and the normalization constant $C_{d_{\text{int}}} = (2\pi)^{d_{\text{int}}/2}$. Under the learned pairwise MMD distances between graphs, $d_{\text{int}} = 1$, making $C_{d_{\text{int}}} = \sqrt{2\pi}$.

The multi-scale design with bandwidths $H_{KDE} = \{h_k\}_{k=1}^M$ enables our model to capture patterns at different granularities, while the learnable weights automatically determine each scale’s importance for the dataset. Building on our structure-aware sample generation mechanism, we train our model by maximizing the density ratio between normal graphs and their perturbed counterparts:

$$\min_{\boldsymbol{\theta}, \boldsymbol{\alpha}} \mathcal{L} := - \sum_{i=1}^N \sum_{j=1}^{N_{\text{pert}}} \frac{\hat{f}_{KDE}(G_i) - \hat{f}_{KDE}(\tilde{G}_i^{(j)})}{\hat{f}_{KDE}(G_i)} \quad (9)$$

where the objective encourages higher density values for normal graphs compared to their perturbed versions. The parameters $\boldsymbol{\theta}$ control the MMD metric learning while $\boldsymbol{\alpha}$ determines the kernel mixing weights. Note that \hat{f}_{KDE} is a realization of $p_{\boldsymbol{\theta}}$ in (1). The rationale of (9) is that **the density of a perturbed graph is often lower than that of the original graph** and the model should be able to recognize this nature. Importantly, $\tilde{G}_i^{(j)}$ may not be anomalous and hence cannot be regarded as a negative sample and used in the manner of contrastive learning [You *et al.*, 2020; Xu *et al.*, 2021].

During inference, we compute anomaly scores as $s(G) = -\hat{f}_{KDE}(G)$, with higher scores indicating higher likelihood of being anomalous. The detection threshold τ is estimated as the negative γ_{TH} -th percentile of reference set densities:

$$\tau = -\text{Percentile}_{\gamma_{TH}} \{ \hat{f}_{KDE}(G_i) \mid G_i \in \mathcal{G}_{ref} \} \quad (10)$$

where γ_{TH} controls the expected anomaly rate (empirically, we use $\gamma_{TH} = 0.1$). The complete algorithm is provided in Algorithm 3 with implementation details in Appendix D.

4 Theoretical Analysis

We provide theoretical guarantees for LGKDE under the following assumptions:

Assumption 4.1. **i)** The GNN Φ_θ has bounded weights $\|W^{(l)}\|_F \leq B_W$. **ii)** The true density f^* is bounded and has bounded second derivatives.

We analyze statistical consistency, convergence rates, and robustness to perturbations. Due to the space limitation, all proofs, auxiliary lemmas and extended discussions are provided in Appendices E. Computational and sample complexity analyses are also provided in Appendix E.5 and E.6.

4.1 Consistency and Convergence

Theorem 4.2 (Consistency of LGKDE). *Under Assumption 4.1, if the KDE bandwidths satisfy $h_k \rightarrow 0$ and $Nh_k^{d_{int}} \rightarrow \infty$ as $N \rightarrow \infty$ for all $k = 1, \dots, M$, then $\hat{f}_{KDE} \xrightarrow{P} f^*$ in L_1 norm.*

Proof in Appendix E.2. This result establishes that LGKDE converges to the true underlying graph density function f^* as the number of samples increases. We further quantify the rate of convergence:

Theorem 4.3 (Convergence Rate). *Under the conditions of Theorem 4.2, the Mean Integrated Squared Error (MISE) of LGKDE with optimal bandwidths $h^* \sim N^{-1/(4+d_{int})}$ achieves:*

$$\mathbb{E} \int_{\mathbb{G}} (\hat{f}_{KDE}^*(G) - f^*(G))^2 d\mathbb{P}^*(G) = O(N^{-\frac{4}{4+d_{int}}}) \quad (11)$$

Proof in Appendix E.3. This rate matches the minimax optimal rate for nonparametric density estimation in d_{int} dimensions, when utilizing the pairwise MMD distance for KDE, MISE bounded to $O(N^{-0.8})$ for $d_{int} = 1$, demonstrating the statistical efficiency of our approach.

4.2 Robustness Analysis

Robustness ensures that LGKDE's density estimate \hat{f}_{KDE} is stable against small changes in input graphs. Detailed in Appendix E.4, we introduce our three main results as follows.

First, Theorem E.4 establishes that \hat{f}_{KDE} is Lipschitz continuous with respect to the learned graph metric d_{MMD} . Specifically, for any two graphs G_1, G_2 , the change $|\hat{f}_{KDE}(G_1) - \hat{f}_{KDE}(G_2)|$ is bounded by $L_{KDE} \cdot d_{12} + C_{KDE} \cdot d_{12}^2 + o(d_{12}^2)$, where $d_{12} = d_{MMD}|\theta(G_1, G_2)$. The constants $L_{KDE} = O(\frac{1}{h_{min}})$, and $C_{KDE} = O(\frac{1}{h_{min}^3})$ (detailed in E.4 and h_{min} is the minimum bandwidth of H_{KDE}) depend on the multi-scale KDE kernel.

Second, Proposition E.5 quantifies the stability of the learned metric d_{MMD} itself under graph perturbations. It shows that for a graph G and its perturbed version \tilde{G} , the induced MMD distance $d_{MMD}|\theta(G, \tilde{G})$ is bounded by $\Delta_{perturb}$ (Proof in Appendix E.5) as follows,

$$d_{MMD}|\theta(G, \tilde{G}) \leq \Delta_{perturb} = O \left(\sqrt{\gamma_{max}} \cdot (B_W)^L \cdot \left(\sqrt{r_{swap}} + \frac{n \cdot \sqrt{p_{pert}} \cdot \sigma_{max} \cdot \max(|r-1|, |1/r-1|)}{d_{min}^2} \right) \right) \quad (12)$$

depends on Φ_θ (layer number L and weight bound $B_W \geq \|\mathbf{W}^{(l)}\|_F$), MMD kernel parameters $\gamma_{max} \in \Gamma_{emb}$, graph properties (size n , minimum degree d_{min} , maximum singular value σ_{max}), and graph perturbation parameters (p_{pert} fraction of total singular values is modified with ratio r).

Finally, Corollary E.6 combines these results to provide our main robustness guarantee for LGKDE against graph-level perturbations:

$$|\hat{f}_{KDE}(G) - \hat{f}_{KDE}(\tilde{G})| \leq L_{KDE} \cdot \Delta_{perturb} + C_{KDE} \cdot \Delta_{perturb}^2 + o(\Delta_{perturb}^2) = O(h_{min}^{-1} \Delta_{perturb} + h_{min}^{-3} \Delta_{perturb}^2) \quad (13)$$

This result confirms that the change in KDE estimates is controllably small and bounded under the $\Delta_{perturb}$, thereby theoretically supporting the stability of LGKDE and our contrastive learning objective Eq. (9).

5 Experiments

We conduct comprehensive experiments to rigorously evaluate the proposed LGKDE framework. We begin by directly assessing LGKDE’s capability in recovering underlying graph distributions on synthetic data where the ground truth is known. Subsequently, acknowledging the intricate nature of real-world graph distributions (e.g., in molecular structures and social networks), which poses significant challenges for direct density modeling, we leverage graph anomaly detection as a primary application to validate LGKDE’s effectiveness against state-of-the-art methods.

5.1 Validating Density Estimation Capabilities on Synthetic Data

To establish LGKDE’s fundamental ability to perform density estimation, we first conducted targeted experiments on synthetic Erdős–Rényi (ER) graphs. In this controlled setting, the true generative parameters of the graphs were known. We generated ER graphs where node counts n were sampled uniformly from [20, 50] and edge probabilities p were drawn from a Beta(2,2) distribution, which is unimodal and peaked at $p = 0.5$. LGKDE was tasked with estimating the density of these graphs.

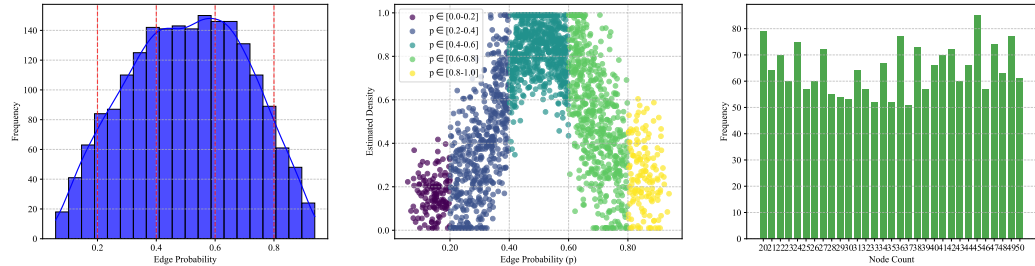


Figure 4: Density estimation results on synthetic Erdős–Rényi graphs. Left: Ground truth Beta(2, 2) distribution for edge probability p . Middle: Learned density estimate from LGKDE versus edge probability p , showing the expected peak around $p = 0.5$. Right: Distribution of node counts (uniform as generated).

As Fig. 4 shows, our results demonstrate that LGKDE successfully recovered the underlying distribution of edge probabilities, assigning significantly higher densities to graphs with p around 0.5 (with Avg. $p \in [0.4 - 0.6] = 0.82$, details in Table 7 of Appendix A.4.1), irrespective of variations in node count. This foundational validation provides strong evidence that LGKDE can capture the true generative process and supports its application to the following more complex, real-world graph data anomaly detection tasks.

5.2 Graph Anomaly Detection on Real-World Benchmarks

5.2.1 Experimental Settings

Datasets: We use eleven widely adopted graph benchmark datasets from the TU Database [Morris *et al.*, 2020]. Following the class-based anomaly detection setup from established practices like [Liu *et al.*, 2023a; Qiao *et al.*, 2024; Wang *et al.*, 2024], minority classes are treated as anomalous, and the majority as normal. Detailed statistics are in Appendix 4.

Baselines: LGKDE is compared against **traditional methods (Graph Kernel + Detector, e.g., WL [Shervashidze *et al.*, 2011] with iForest [Liu *et al.*, 2008])** and various **GNN-based deep learning approaches: OCGIN [Zhao and Akoglu, 2021], GLocalKD [Ma *et al.*, 2022], OCGTL [Qiu *et al.*, 2022], SIGNET [Liu *et al.*, 2023b], GLADC [Luo *et al.*, 2022], and CVTGAD [Li *et al.*, 2023].** Full descriptions of baselines are in Appendix F.4.

Implementation Details: LGKDE is implemented in PyTorch, using a GCN backbone and the Adam optimizer with a learning rate of 0.001. For multi-scale KDE, we use $M = 5$ bandwidths. For fair comparison, all GNN-based baselines use a similar GNN architecture where applicable, adhering to settings from unified benchmarks [Wang *et al.*, 2024]. Further details on LGKDE’s specific hyperparameter settings and those for baselines are in Appendix F.3 and Appendix F.4. All results are averaged over 5 trials.

Table 1: Comparison in terms of AUROC \uparrow . The **bold**, **purple** and **orange** numbers denote the best, second best, and third best performances, respectively. “Avg. AUROC” and “Avg. Rank” indicate the average AUROC and rank across all datasets.

Dataset	Graph Kernel + Detector				GNN-based Deep Learning Methods					Proposed Method	
	PK-SVM	PK-iF	WL-SVM	WL-iF	OCGIN	GLocalKD	OCGTL	SIGNET	GLADC	CVTGAD	
MUTAG	46.06 \pm 0.47	47.98 \pm 0.41	62.18 \pm 0.29	65.71 \pm 0.38	79.55 \pm 0.22	86.25 \pm 0.57	88.02\pm0.43	88.84\pm0.15	83.07 \pm 0.29	86.64 \pm 0.32	91.63\pm0.31
PROTEINS	49.43 \pm 0.69	61.24 \pm 0.34	53.85 \pm 0.26	65.75 \pm 0.35	76.46 \pm 0.13	77.29\pm0.41	72.89 \pm 0.57	75.86 \pm 0.30	77.43\pm0.19	76.49 \pm 0.29	78.97\pm0.26
DD	47.69 \pm 0.24	75.29 \pm 0.46	47.98 \pm 0.32	70.49 \pm 0.28	79.08\pm0.19	80.76\pm0.50	77.76 \pm 0.48	74.53 \pm 0.11	76.54 \pm 0.25	78.84 \pm 0.40	79.84\pm0.41
ENZYMES	52.45 \pm 0.29	49.82 \pm 0.67	53.79 \pm 0.34	51.03 \pm 0.42	62.44 \pm 0.38	61.75 \pm 0.10	63.59\pm0.11	63.12 \pm 0.52	63.44 \pm 0.30	68.56\pm0.43	71.04\pm0.45
DHFR	48.31 \pm 0.47	52.79 \pm 0.35	50.30 \pm 0.31	51.64 \pm 0.22	61.09 \pm 0.27	61.79 \pm 0.54	59.82 \pm 0.44	72.87\pm0.28	61.25 \pm 0.19	63.23\pm0.38	82.58\pm0.33
BZR	46.67 \pm 0.52	59.08 \pm 0.29	51.16 \pm 0.36	51.71 \pm 0.45	69.13 \pm 0.13	68.55 \pm 0.15	51.89 \pm 0.44	80.79\pm0.38	68.23 \pm 0.31	77.69\pm0.28	81.11\pm0.32
COX2	52.19 \pm 0.16	52.48 \pm 0.38	53.34 \pm 0.27	49.56 \pm 0.11	57.81 \pm 0.50	58.93 \pm 0.47	59.81 \pm 0.38	72.35\pm0.58	64.13 \pm 0.23	64.36\pm0.16	66.69\pm0.39
AIDS	50.93 \pm 0.19	52.01 \pm 0.53	52.56 \pm 0.41	61.42 \pm 0.50	96.89 \pm 0.20	96.93 \pm 0.34	99.36\pm0.67	97.60 \pm 0.28	98.02 \pm 0.23	99.21\pm0.27	99.06\pm0.25
IMDB-B	51.75 \pm 0.30	52.83 \pm 0.51	52.98 \pm 0.69	51.79 \pm 0.32	61.47 \pm 0.18	53.31 \pm 0.53	65.27 \pm 0.24	70.12\pm0.61	65.94 \pm 0.26	69.82\pm0.13	68.77\pm0.29
NCI1	51.39 \pm 0.19	50.22 \pm 0.12	54.18 \pm 0.67	50.41 \pm 0.31	69.46 \pm 0.36	65.29 \pm 0.21	75.75\pm0.47	74.32\pm0.34	68.32 \pm 0.22	69.13 \pm 0.58	76.67\pm0.30
COLLAB	49.72 \pm 0.60	51.38 \pm 0.20	54.62 \pm 1.28	51.41 \pm 0.39	60.58 \pm 0.27	51.85 \pm 0.18	48.13 \pm 0.41	72.45\pm0.11	54.32 \pm 0.37	71.01\pm0.58	67.94\pm0.41
Avg. AUROC	50.60	55.92	53.35	56.45	70.36	69.34	69.30	76.62	70.97	75.00	78.57
Avg. Rank	10.45	9.09	8.64	9.09	5.36	5.27	5.18	3.27	4.82	3.09	1.73

Evaluation Metrics: Performance is assessed using Area Under the ROC Curve (AUROC), Area Under the Precision-Recall Curve (AUPRC), and False Positive Rate at 95% True Positive Rate (FPR95). Higher(\uparrow) AUROC/AUPRC and lower(\downarrow) FPR95 indicate better performance. Metric definitions are in Appendix F.2.

5.2.2 Main Results and Analysis

Table 1 presents the AUROC. AUPRC and FPR95 results are in Appendix A.3 (Tables 5 and 6).

Overall Performance. LGKDE consistently demonstrates superior performance, achieving the highest average AUROC (78.57%) and AUPRC (87.69%). These results outperform strong baselines like SIGNET and CVTGAD, particularly on datasets such as DHFR (AUROC: 82.58% vs. SIGNET’s 72.87% and CVTGAD’s 63.23%). LGKDE also obtains the best average FPR95 (61.62%, Table 6). This underscores LGKDE’s efficacy in modeling complex normal graph distributions to detect anomalies.

Method-specific Analysis. Traditional graph kernel methods generally underperform, reflecting the limitations of fixed, handcrafted kernels. Deep learning methods show improvements, though one-class approaches like OCGIN can be constrained by their distributional assumptions. LGKDE’s end-to-end learning of both the metric space and density estimator offers a distinct advantage over two-stage methods (with extra comparison on InfoGraph [Sun *et al.*, 2019a] and GAE [Kipf and Welling, 2016] followed by a separate KDE), as evidenced by its significantly better performance on MUTAG (e.g., 91.63% AUROC vs. 81.94% for GAE+KDE; details in Table 8). This joint optimization allows LGKDE to learn a metric space more attuned to the density estimation task. Moreover, LGKDE exhibits resilience; it maintains a clear density separation between true normal and anomalous graphs even when the training data is contaminated with anomalous samples, demonstrating robust learning of meaningful density characteristics (details in A.4.3, Figure 8, Table 9, and Ablation 5.3).

Dataset-specific Insights and Learned Representations. LGKDE excels on molecular datasets (e.g., MUTAG, PROTEINS), indicating its proficiency in capturing intricate chemical structures. This is supported by t-SNE visualizations (Figure 6) on MUTAG, which show LGKDE learning a more discriminative embedding space with clearer class separation compared to other methods. Qualitative analysis of graphs from MUTAG corresponding to “average”, highest, and lowest learned densities (Appendix A.4.4, Figure 9) further reveals that LGKDE captures structurally meaningful patterns: high-density graphs often exhibit complex ring structures typical of the normal class, while low-density graphs display simpler or atypical formations. On social network datasets (e.g., IMDB-B, COLLAB), LGKDE remains competitive, demonstrating its adaptability.

5.3 Ablation Studies

We conduct comprehensive ablation studies to analyze the impact of various components and hyper-parameters in LGKDE on the MUTAG Dataset. Table 2 and Figure 5 present the results on several key aspects:

Multi-scale KDE Impact As shown in Table 2, removing the multi-scale KDE component leads to significant performance degradation. Single bandwidth variants exhibit varying performance levels, with optimal performance at moderate bandwidth values ($h = 0.1$) achieving 86.92% AUROC, still

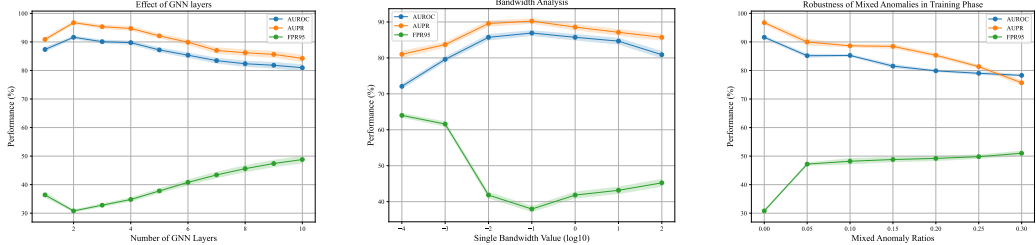


Figure 5: Ablation Studies on MUTAG Dataset

Table 2: Ablation study on key components of LGKDE. Results are reported as mean(%) \pm std(%) over 5 runs.

Variant		AUROC	AUPRC	FPR95
w/o Multi-scale KDE	$h = 0.01$	85.73 ± 0.45	89.56 ± 0.43	41.82 ± 0.48
	$h = 0.1$	86.92 ± 0.41	90.24 ± 0.38	37.95 ± 0.43
	$h = 1.0$	85.73 ± 0.45	88.56 ± 0.43	41.82 ± 0.48
	$h = 10.0$	84.67 ± 0.48	87.12 ± 0.46	43.15 ± 0.52
	$h = 100.0$	80.89 ± 0.52	85.73 ± 0.49	45.23 ± 0.55
w/o MMD Distance	Graph Readout (avg)	83.89 ± 0.49	86.92 ± 0.47	44.73 ± 0.53
	Graph Readout (sum)	84.73 ± 0.48	87.56 ± 0.46	43.82 ± 0.52
w/o Learnable Weights		88.92 ± 0.43	89.64 ± 0.41	36.97 ± 0.45
Full model of LGKDE		91.63 ± 0.31	96.75 ± 0.35	30.80 ± 0.27

notably below the full model’s 91.63%. This validates the effectiveness of our multi-scale approach in capturing graph patterns at different granularities.

GNN Layer Analysis Figure 5(upper) shows the impact of GNN layer depth on model performance. Performance peaks at 2 layers (91.63% AUROC, 96.75% AUPRC) before gradually declining, indicating the onset of over-smoothing at deeper architectures. This suggests that moderate-depth GNNs are sufficient for capturing relevant structural information while avoiding over-smoothing effects.

Bandwidth Sensitivity Figure 5(middle) illustrates how single bandwidth values affect performance. The model shows optimal performance in the range of 0.01-1.0, with significant degradation at extreme values. This demonstrates the importance of appropriate bandwidth selection and justifies our multi-scale approach with learnable weights.

Robustness to Training Contamination and Density Separation Figure 5(bottom) examines model robustness when training data is contaminated with anomalous samples. Performance remains relatively stable up to 10% contamination (85.26% AUROC) before showing noticeable degradation at higher ratios. Complementary experiments analyzing the density gap between known normal and anomalous samples under varying contamination levels further confirm the model’s ability to learn a meaningful density separation, even with polluted training data (see Appendix A.4.3 and Figure 8). This demonstrates the model’s resilience to moderate levels of training data pollution, although maintaining clean training data is preferable for optimal performance.

MMD Distance and Learnable Weights: Replacing the MMD distance with simple graph readouts results in approximately 7% AUROC degradation. Similarly, removing learnable bandwidth weights leads to a 2.7% AUROC decrease, highlighting the importance of adaptive multi-scale modeling. These results validate the key design choices in our framework.

6 Conclusion

We proposed LGKDE, a novel framework for learnable kernel density estimation on graphs, which jointly optimizes graph representations and multi-scale kernel parameters via maximizing the density of normal graphs relative to their well-designed perturbed counterparts. Theoretical analysis and extensive experiments validate LGKDE’s effectiveness and superior performance in graph density estimation and anomaly detection.

References

Leman Akoglu, Hanghang Tong, and Danai Koutra. Graph based anomaly detection and description: a survey. *Data mining and knowledge discovery*, 29(3):626–688, 2015.

Mennatallah Amer, Markus Goldstein, and Slim Abdennadher. Enhancing one-class support vector machines for unsupervised anomaly detection. In *Proceedings of the ACM SIGKDD workshop on outlier detection and description*, pages 8–15, 2013.

Kendall Atkinson and Weimin Han. *Theoretical numerical analysis*, volume 39. Springer, 2005.

John Adrian Bondy, Uppaluri Siva Ramachandra Murty, et al. *Graph theory with applications*, volume 290. Macmillan London, 1976.

Karsten M Borgwardt and Hans-Peter Kriegel. Shortest-path kernels on graphs. In *Fifth IEEE international conference on data mining*, pages 74–81, 2005.

Jinyu Cai, Yunhe Zhang, Jicong Fan, and See-Kiong Ng. Lg-fgad: An effective federated graph anomaly detection framework. In *Proceedings of the International Joint Conference on Artificial Intelligence*, 2024.

Kaize Ding, Jundong Li, Rohit Bhanushali, and Huan Liu. Deep anomaly detection on attributed networks. In *Proceedings of the 2019 SIAM International Conference on Data Mining*, pages 594–602, 2019.

Richard M Dudley. *Uniform central limit theorems*, volume 142. Cambridge university press, 2014.

Federico Errica, Davide Bacciu, and Alessio Micheli. Graph mixture density networks. *ArXiv*, abs/2012.03085, 2020.

Matthias Fey and Jan Eric Lenssen. Fast graph representation learning with pytorch geometric. *arXiv preprint arXiv:1903.02428*, 2019.

Justin Gilmer, Samuel S Schoenholz, Patrick F Riley, Oriol Vinyals, and George E Dahl. Neural message passing for quantum chemistry. In *International conference on machine learning*, pages 1263–1272, 2017.

Evarist Giné and Richard Nickl. Uniform limit theorems for wavelet density estimators. *The Annals of Probability*, 37(4), July 2009.

Arthur Gretton, Karsten M Borgwardt, Gunnar Rätsch, Alexander J Smola, and Bernhard Schölkopf. A kernel two-sample test. In *Advances in neural information processing systems*, pages 1299–1307, 2012.

Aditya Grover and Jure Leskovec. node2vec: Scalable feature learning for networks. In *Proceedings of the 22nd ACM SIGKDD international conference on Knowledge discovery and data mining*, pages 855–864, 2016.

Will Hamilton, Zhitao Ying, and Jure Leskovec. Inductive representation learning on large graphs. In *Advances in neural information processing systems*, volume 30, 2017.

William L Hamilton. *Graph representation learning*. Morgan & Claypool Publishers, 2020.

Nicholas J Higham. *Functions of matrices: theory and computation*. SIAM, 2008.

Ming Jin, Yixin Liu, Yu Zheng, Lianhua Chi, Yuan-Fang Li, and Shirui Pan. Anemone: Graph anomaly detection with multi-scale contrastive learning. In *Proceedings of the 30th ACM international conference on information & knowledge management*, pages 3122–3126, 2021.

Wei Jin, Yao Ma, Yiqi Wang, Xiaorui Liu, Jiliang Tang, Yukuo Cen, Jie Tang, Chuan Shi, Yanfang Ye, Jiawei Zhang, and Philip S. Yu. Graph representation learning: Foundations, methods, applications and systems. *Proceedings of the 27th ACM SIGKDD Conference on Knowledge Discovery & Data Mining*, 2021.

Peter Kairouz, H Brendan McMahan, Brendan Avent, Aurélien Bellet, Mehdi Bennis, Arjun Nitin Bhagoji, Kallista Bonawitz, Zachary Charles, Graham Cormode, Rachel Cummings, et al. Advances and open problems in federated learning. *Foundations and Trends® in Machine Learning*, 14(1–2):1–210, 2021.

Hisashi Kashima, Koji Tsuda, and Akihiro Inokuchi. Marginalized kernels between labeled graphs. In *Proceedings of the 20th international conference on machine learning (ICML-03)*, pages 321–328, 2003.

Thomas N Kipf and Max Welling. Variational graph auto-encoders. *arXiv preprint arXiv:1611.07308*, 2016.

Thomas N Kipf and Max Welling. Semi-supervised classification with graph convolutional networks. In *International Conference on Learning Representations*, 2017.

Tommaso Lanciano, Francesco Bonchi, and Aristides Gionis. Explainable classification of brain networks via contrast subgraphs. In *Proceedings of the 26th ACM SIGKDD International Conference on Knowledge Discovery & Data Mining*, pages 3308–3318, 2020.

Zenan Li, Qitian Wu, Fan Nie, and Junchi Yan. Graphde: A generative framework for debiased learning and out-of-distribution detection on graphs. *Advances in Neural Information Processing Systems*, 35:30277–30290, 2022.

Jindong Li, Qianli Xing, Qi Wang, and Yi Chang. Cvtgad: Simplified transformer with cross-view attention for unsupervised graph-level anomaly detection. In *Joint European Conference on Machine Learning and Knowledge Discovery in Databases*, pages 185–200. Springer, 2023.

Fei Tony Liu, Kai Ming Ting, and Zhi-Hua Zhou. Isolation forest. In *2008 eighth ieee international conference on data mining*, pages 413–422. IEEE, 2008.

Jenny Liu, Aviral Kumar, Jimmy Ba, Jamie Kiros, and Kevin Swersky. Graph normalizing flows. In *Advances in neural information processing systems*, pages 13578–13588, 2019.

Bowen Liu, Yutao Liu, Bozitao Liu, and Xiaolin Wang. Energy-based models for atomic-resolution protein conformations. In *International Conference on Learning Representations*, 2020.

Yixin Liu, Kaize Ding, Huan Liu, and Shirui Pan. Good-d: On unsupervised graph out-of-distribution detection. In *Proceedings of the 16th ACM International Conference on Web Search and Data Mining*, pages 339–347, 2023.

Yixin Liu, Kaize Ding, Qinghua Lu, Fuyi Li, Leo Yu Zhang, and Shirui Pan. Towards self-interpretable graph-level anomaly detection. *Advances in Neural Information Processing Systems*, 36, 2023.

Xuexiong Luo, Jia Wu, Jian Yang, Shan Xue, Hao Peng, Chuan Zhou, Hongyang Chen, Zhao Li, and Quan Z Sheng. Deep graph level anomaly detection with contrastive learning. *Scientific Reports*, 12(1):19867, 2022.

Xiaoxiao Ma, Jia Wu, Shan Xue, Jian Yang, Chuan Zhou, Quan Z Sheng, Hui Xiong, and Leeman Akoglu. A comprehensive survey on graph anomaly detection with deep learning. *IEEE Transactions on Knowledge and Data Engineering*, 2021.

Rongrong Ma, Guansong Pang, Ling Chen, and Anton van den Hengel. Deep graph-level anomaly detection by glocal knowledge distillation. In *Proceedings of the Fifteenth ACM International Conference on Web Search and Data Mining*, pages 704–714, 2022.

Christopher Morris, Nils M Kriege, Franka Bause, Kristian Kersting, Petra Mutzel, and Marion Neumann. Tudataset: A collection of benchmark datasets for learning with graphs. *arXiv preprint arXiv:2007.08663*, 2020.

Giulia Muzio, Leslie O’Bray, and Karsten Borgwardt. Biological network analysis with deep learning. *Briefings in Bioinformatics*, 22:1515–1530, 2020.

B. Nachman and D. Shih. Anomaly detection with density estimation. *Physical Review D*, 101:075042, 2020.

Marion Neumann, Roman Garnett, Christian Bauckhage, and Kristian Kersting. Propagation kernels: efficient graph kernels from propagated information. *Machine Learning*, 102:209–245, 2016.

Guansong Pang, Chunhua Shen, Longbing Cao, and Anton Van Den Hengel. Deep learning for anomaly detection: A review. *ACM computing surveys (CSUR)*, 54(2):1–38, 2021.

Bryan Perozzi, Rami Al-Rfou, and Steven Skiena. Deepwalk: Online learning of social representations. In *Proceedings of the 20th ACM SIGKDD international conference on Knowledge discovery and data mining*, pages 701–710, 2014.

Hezhe Qiao, Hanghang Tong, Bo An, Irwin King, Charu Aggarwal, and Guansong Pang. Deep graph anomaly detection: A survey and new perspectives. *arXiv preprint arXiv:2409.09957*, 2024.

Chen Qiu, Marius Kloft, Stephan Mandt, and Maja Rudolph. Raising the bar in graph-level anomaly detection. In *Proceedings of the Thirty-First International Joint Conference on Artificial Intelligence*, pages 2196–2203, 2022.

Y. Rong, Tingyang Xu, Junzhou Huang, Wenbing Huang, Hong Cheng, Yao Ma, Yiqi Wang, Tyler Derr, Lingfei Wu, and Tengfei Ma. Deep graph learning: Foundations, advances and applications. *Proceedings of the 26th ACM SIGKDD International Conference on Knowledge Discovery & Data Mining*, 2020.

Xu Shen, Yili Wang, Kaixiong Zhou, Shirui Pan, and Xin Wang. Optimizing ood detection in molecular graphs: A novel approach with diffusion models. In *Proceedings of the 30th ACM SIGKDD Conference on Knowledge Discovery and Data Mining*, pages 2640–2650, 2024.

Nino Shervashidze, Pascal Schweitzer, Erik Jan Van Leeuwen, Kurt Mehlhorn, and Karsten M Borgwardt. Weisfeiler-lehman graph kernels. *Journal of Machine Learning Research*, 12(Sep):2539–2561, 2011.

Giannis Siglidis, Giannis Nikolentzos, Stratis Limnios, Christos Giatsidis, Konstantinos Skianis, and Michalis Vazirgiannis. Grakel: A graph kernel library in python, 2020.

Yan Sun and Jicong Fan. Mmd graph kernel: Effective metric learning for graphs via maximum mean discrepancy. In *The Twelfth International Conference on Learning Representations*, 2024.

Fan-Yun Sun, Jordan Hoffmann, Vikas Verma, and Jian Tang. Infograph: Unsupervised and semi-supervised graph-level representation learning via mutual information maximization. *arXiv preprint arXiv:1908.01000*, 2019.

Mengying Sun, Sendong Zhao, Coryandar Gilvary, Olivier Elemento, Jiayu Zhou, and Fei Wang. Graph convolutional networks for computational drug development and discovery. *Briefings in Bioinformatics*, 2019.

Ziheng Sun, Xudong Wang, Chris Ding, and Jicong Fan. Learning graph representation via graph entropy maximization. In Ruslan Salakhutdinov, Zico Kolter, Katherine Heller, Adrian Weller, Nuria Oliver, Jonathan Scarlett, and Felix Berkenkamp, editors, *Proceedings of the 41st International Conference on Machine Learning*, volume 235 of *Proceedings of Machine Learning Research*, pages 47133–47158. PMLR, 21–27 Jul 2024.

Laurens Van der Maaten and Geoffrey Hinton. Visualizing data using t-sne. *Journal of machine learning research*, 9(11), 2008.

Petar Velickovic, William Fedus, William L Hamilton, Pietro Liò, Yoshua Bengio, and R Devon Hjelm. Deep graph infomax. *ICLR (Poster)*, 2(3):4, 2019.

S Vichy N Vishwanathan, Nicol N Schraudolph, Risi Kondor, and Karsten M Borgwardt. Graph kernels. *Journal of Machine Learning Research*, 11(Apr):1201–1242, 2010.

Martin J Wainwright. *High-dimensional statistics: A non-asymptotic viewpoint*, volume 48. Cambridge university press, 2019.

Li Wang and Ren-Cang Li. Learning low-dimensional latent graph structures: A density estimation approach. *IEEE Transactions on Neural Networks and Learning Systems*, 31:1098–1112, 2020.

Yuyang Wang, Zijie Li, and Amir Farimani. Graph neural networks for molecules. *ArXiv*, abs/2209.05582, 2022.

Yili Wang, Yixin Liu, Xu Shen, Chenyu Li, Kaize Ding, Rui Miao, Ying Wang, Shirui Pan, and Xin Wang. Unifying unsupervised graph-level anomaly detection and out-of-distribution detection: A benchmark. *arXiv preprint arXiv:2406.15523*, 2024.

Minjie Yu Wang. Deep graph library: Towards efficient and scalable deep learning on graphs. In *ICLR workshop on representation learning on graphs and manifolds*, 2019.

Larry Wasserman. *All of nonparametric statistics*. Springer Science & Business Media, 2006.

Zonghan Wu, Shirui Pan, Fengwen Chen, Guodong Long, Chengqi Zhang, and S Yu Philip. A comprehensive survey on graph neural networks. *IEEE transactions on neural networks and learning systems*, 32(1):4–24, 2020.

Han Xie, Jing Ma, Li Xiong, and Carl Yang. Federated graph classification over non-iid graphs. *Advances in Neural Information Processing Systems*, 34:18839–18852, 2021.

Keyulu Xu, Weihua Hu, Jure Leskovec, and Stefanie Jegelka. How powerful are graph neural networks? In *International Conference on Learning Representations*, 2019.

Dongkuan Xu, Wei Cheng, Dongsheng Luo, Haifeng Chen, and Xiang Zhang. Infogcl: Information-aware graph contrastive learning. *Advances in Neural Information Processing Systems*, 34:30414–30425, 2021.

Yuning You, Tianlong Chen, Yongduo Sui, Ting Chen, Zhangyang Wang, and Yang Shen. Graph contrastive learning with augmentations. *Advances in neural information processing systems*, 33:5812–5823, 2020.

Ge Zhang, Zhenyu Yang, Jia Wu, Jian Yang, Shan Xue, Hao Peng, Jianlin Su, Chuan Zhou, Quan Z Sheng, Leman Akoglu, et al. Dual-discriminative graph neural network for imbalanced graph-level anomaly detection. *Advances in Neural Information Processing Systems*, 35:24144–24157, 2022.

Lingxiao Zhao and Leman Akoglu. Using classification datasets to evaluate graph outlier detection: Peculiar observations and new insights. *Big Data*, 2021.

Symbol and Notation

This appendix provides a comprehensive reference (Table 3) for the principal notation used throughout the paper. While we strive to maintain consistent notation, specialized symbols that appear exclusively in proofs or specific derivations are defined in their respective contexts. We adhere to the following conventions:

- bold uppercase letters (e.g., \mathbf{A} , \mathbf{X}) denote matrices; bold lowercase letters (e.g., \mathbf{z}) represent vectors;
- calligraphic letters (e.g., \mathcal{G} , \mathcal{H}) indicate sets or spaces; uppercase letters (e.g., G , N) typically represent graphs, counts, or constants; lowercase letters (e.g., h , d) typically represent scalar values or functions; and Greek letters (e.g., γ , π) denote parameters or functional elements.
- Superscripts and subscripts are used to index specific instances (e.g., G_i for the i -th graph) or to indicate special properties or variants of a symbol.

Table 3: Summary of Notation and Symbols

Symbol(s)	Description
\mathbb{G}	Space of attributed graphs.
$G_i = (V_i, E_i, \mathbf{X}_i)$	Graph i with nodes V_i , edges E_i , and node features \mathbf{X}_i .
$\mathbf{A}_i, \mathbf{X}_i, n_i$	Adjacency matrix, feature matrix (d_{in} -dim), and node count for G_i .
\tilde{G}	Perturbed version of a graph G .
$\hat{\mathbf{A}}$	Normalized adjacency matrix: $\mathbf{D}^{-1/2}(\mathbf{A} + \mathbf{I})\mathbf{D}^{-1/2}$.
$\mathcal{S}_h, \mathcal{S}_m, \mathcal{S}_l; E(k); \tau_1, \tau_2$	Singular value sets, cumulative energy, and thresholds for spectral perturbation.
$r_{swap}, p_{pert}, flag$	Ratio of nodes for feature swapping; the fraction of singular values be modified; edge operation $flag \in \{0, 1\}$ (0: removal, 1: addition)
\mathbb{P}^*, f^*	True underlying probability measure and density function of graphs.
\hat{f}_{KDE}	Estimated KDE density function for graphs.
$\mu, P_{\mathbf{Z}}$	Base measure on \mathbb{G} ; Empirical distribution of node embeddings.
θ, Φ_{θ}	GNN parameters ($\{\mathbf{W}^{(l)}\}_{l=1}^L$) and the GNN encoder.
$\mathbf{Z}_i, \mathbf{z}_p^{(i)}$	Node embedding matrix for G_i ($\in \mathbb{R}^{n_i \times d_{out}}$), and embedding of p -th node in G_i .
d_{hid} and d_{out} , $\mathbf{W}^{(l)}$, L	GNN hidden and output dimension, l -th layer weights, number of GNN layers.
d_{MMD}	MMD distance between graphs.
$\mathcal{K}_{emb}, k_{emb}, \gamma, \Gamma_{emb}$	Family of MMD kernels (k_{emb} , typically Gaussian) acting on node embeddings, its bandwidth γ , and set of S hyperparameters $\Gamma_{emb} = \{\gamma_s\}_{s=1}^S$.
$\mathcal{H}, \mu_{\delta_{\mathbf{z}}}, \mu_{P_{\mathbf{Z}}}, \mathcal{M}$	RKHS for k_{emb} ; Kernel mean embedding of a Dirac delta and of distribution $P_{\mathbf{Z}}$; Riemannian manifold induced by the MMD metric.
K_{KDE}, K_0, h, H_{KDE}	KDE kernel function (profile K_0 , typically Gaussian) operating on d_{MMD} , its bandwidth h , and set of M bandwidths $H_{KDE} = \{h_j\}_{j=1}^M$.
$\alpha, \mathcal{A}, \pi_j, \phi_j$	KDE mixture weight parameters ($\{\alpha_j\}$ in space \mathcal{A}), j -th mixture weight $\pi_j(\alpha)$, and j -th KDE component density ϕ_j .
$d_{int}, C_{d_{int}}$	Intrinsic dimension (set to 1 for KDE on pairwise distances), KDE normalization constant.
\mathcal{L}, γ_{TH}	Training loss function; Anomaly rate threshold parameter.
$L_{\mu}(k), L_{\mu}^*$	Lipschitz constant of kernel mean map for $k \in \mathcal{K}_{emb}$, and its supremum.
$L_K(h), L_{KDE}, C_{KDE}$	Lipschitz constant of $K_{KDE}(d, h)$ w.r.t d ; Overall Lipschitz and 2nd-order coefficient for \hat{f}_{KDE} .
$\beta, \epsilon, \Delta_{perturb}$	Smoothness of f^* ; Accuracy in sample complexity; MMD bound from perturbation.
$B_{\Delta X}, B_{\Delta A}, B_{\Delta \hat{A}}, B_W, B_X$	Norm bounds for perturbations and GNN/feature matrices.
$\ \cdot\ _F$	Frobenius norm for matrices, defined as $\ \mathbf{A}\ _F = \sqrt{\sum_{i,j} a_{ij} ^2}$.
$\ \cdot\ _2$	Euclidean norm for vectors; for matrices, denotes the spectral norm (largest singular value).
$\ \cdot\ _{\infty}$	L_{∞} norm: for functions, $\ f\ _{\infty} = \sup_x f(x) $; for vectors, $\ \mathbf{x}\ _{\infty} = \max_i x_i $.
$\ \cdot\ _{\mathcal{H}}$	RKHS norm in the Hilbert space \mathcal{H} induced by kernel k .

A More Experiment Results

A.1 Statistics of Datasets

See Table 4.

Table 4: Statistics of the benchmark datasets.

Dataset	#Graphs	Avg. Nodes	Avg. Edges	#Classes	Anomaly Ratio
MUTAG	188	17.93	19.79	2	33.5%
PROTEINS	1113	39.06	72.82	2	40.5%
DD	1178	284.32	715.66	2	41.7%
ENZYMES	600	32.63	62.14	6	16.7%
DHFR	756	42.43	44.54	2	39.0%
BZR	405	35.75	38.36	2	35.3%
COX2	467	41.22	43.45	2	37.8%
AIDS	2000	15.69	16.20	2	31.2%
IMDB-BINARY	1000	19.77	96.53	2	50.0%
NCI1	4110	29.87	32.30	2	35.1%
COLLAB	5000	74.49	2457.78	3	21.6%

A.2 Visualization and Comparison on MUTAG datasets

See Figure 6 for t-SNE visualizations comparing different representative methods of our benchmarks.

- 1) **Separation Quality:** LGKDE achieves the clearest separation between normal (Class 0) and anomalous (Class 1) graphs, displaying a concentric circular structure with normal samples forming a well-defined core surrounded by anomalous samples. This distinctive pattern aligns with its superior performance (AUROC: 91.63%, AUPRC: 96.75%).
- 2) **Deep Learning Methods:** - SIGNET shows partial separation but with more scattered distribution (AUROC: 88.84%, second best). - OCGTL exhibits some clustering but with significant overlap between classes (AUROC: 88.02%). - OCGIN shows the least structured distribution among deep methods (AUROC: 79.55%).
- 3) **Traditional Kernels:** - WL and PK kernels both show substantial overlap between classes, explaining their relatively poor performance (WL-SVM AUROC: 62.18%, PK-SVM AUROC: 46.06%). - Their t-SNE visualizations lack clear structural patterns, suggesting limited ability to capture meaningful graph similarities.
- 4) **Distribution Structure:** LGKDE’s concentric arrangement suggests it successfully learns a meaningful metric space where normal graphs are tightly clustered while anomalous graphs are naturally pushed toward the periphery. This structure reflects the principle of density estimation where normal patterns should be concentrated in high-density regions. The visualization results strongly correlate with quantitative metrics across all methods, with clearer visual separation corresponding to better performance in AUROC, AUPRC, and FPR95. This demonstrates the effectiveness of our learned kernel approach.

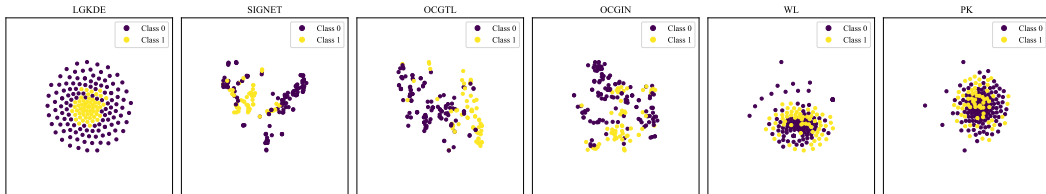


Figure 6: t-SNE visualization (perplexity=30) of learned kernel matrix on MUTAG dataset. For LGKDE, WL and PK, we use learned kernel matrix do SVD get $\mathbf{U}\Sigma\mathbf{V}^T$ and use the $\Sigma\mathbf{V}^T$ as the t-SNE inputs. For SIGNET, OCGTL and OCGIN, we use their learned graph-level readout embeddings as the t-SNE inputs.

A.3 Comparison in terms of AUPRC and FPR95 Results

See Table 5 and Table 6.

Table 5: Comparison in terms of AUPRC \uparrow . The **bold**, **purple** and **orange** numbers denote the best, second best, and third best performances, respectively. “Avg. AUPRC” and “Avg. Rank” indicate the average AUPRC and rank across all datasets.

Dataset	Graph Kernel + Detector				GNN-based Deep Learning Methods					Proposed Method	
	PK-SVM	PK-iF	WL-SVM	WL-iF	OCGIN	GLocalKD	OCGTL	SIGNET	GLADC	CVTGAD	
MUTAG	47.80 \pm 0.25	45.89 \pm 0.21	50.94 \pm 0.25	55.15 \pm 0.22	74.07 \pm 0.24	75.45 \pm 0.28	79.70\pm0.33	77.41 \pm 0.25	72.12 \pm 0.38	81.29\pm0.30	96.75\pm0.35
PROTEINS	44.07 \pm 0.20	31.38 \pm 0.19	43.39 \pm 0.23	48.02 \pm 0.27	79.78 \pm 0.37	76.98 \pm 0.30	70.85 \pm 0.28	75.21 \pm 0.26	81.93\pm0.40	83.92\pm0.35	85.08\pm0.22
DD	45.94 \pm 0.25	16.29 \pm 0.11	41.89 \pm 0.19	46.61 \pm 0.18	84.16\pm0.33	87.45\pm0.39	73.50 \pm 0.21	75.43 \pm 0.25	74.14 \pm 0.28	72.87 \pm 0.30	89.31\pm0.29
ENZYMES	40.83 \pm 0.22	43.65 \pm 0.19	21.56 \pm 0.18	24.14 \pm 0.21	32.67\pm0.30	29.32 \pm 0.24	24.09 \pm 0.18	22.17 \pm 0.12	23.88 \pm 0.21	30.18\pm0.20	97.79\pm0.33
DHFR	45.28 \pm 0.20	40.46 \pm 0.18	30.43 \pm 0.15	34.42 \pm 0.19	50.84\pm0.29	47.32 \pm 0.25	38.92 \pm 0.21	58.64\pm0.35	44.65 \pm 0.23	52.43 \pm 0.30	78.64\pm0.27
BZR	47.04 \pm 0.26	33.70 \pm 0.15	74.22 \pm 0.32	76.27 \pm 0.28	88.32\pm0.33	84.17 \pm 0.28	79.82 \pm 0.25	91.98\pm0.40	83.02 \pm 0.27	90.12 \pm 0.35	88.79 \pm 0.35
COX2	41.15 \pm 0.18	40.80 \pm 0.19	55.41 \pm 0.30	81.08 \pm 0.32	82.95\pm0.35	76.55 \pm 0.29	82.45\pm0.32	86.35\pm0.39	82.47 \pm 0.30	85.23 \pm 0.37	84.98\pm0.28
AIDS	42.46 \pm 0.23	41.30 \pm 0.22	10.97 \pm 0.11	29.69 \pm 0.15	93.42\pm0.37	95.28\pm0.35	97.89\pm0.40	63.58 \pm 0.26	89.43 \pm 0.31	96.35\pm0.38	95.27 \pm 0.13
IMDB-B	41.58 \pm 0.23	40.42 \pm 0.21	49.04 \pm 0.19	59.29 \pm 0.32	60.34 \pm 0.18	54.49 \pm 0.20	58.45 \pm 0.21	67.12\pm0.38	61.72 \pm 0.26	68.89\pm0.35	87.17\pm0.34
NCII	41.97 \pm 0.22	43.22 \pm 0.19	63.42 \pm 0.28	51.60 \pm 0.23	54.19 \pm 0.22	40.15 \pm 0.16	67.45\pm0.32	66.45\pm0.31	48.83 \pm 0.25	65.12 \pm 0.25	92.22\pm0.58
COLLAB	43.76 \pm 0.25	41.98 \pm 0.20	43.12 \pm 0.19	52.15 \pm 0.35	56.97 \pm 0.32	47.89 \pm 0.25	46.11 \pm 0.18	69.24\pm0.40	58.47 \pm 0.22	70.59\pm0.35	68.51\pm0.23
Avg. AUPRC	43.81	38.10	45.85	50.77	68.88	65.00	65.38	68.51	65.51	72.45	87.69
Avg. Rank	8.55	9.55	9.45	7.73	4.55	5.91	5.82	3.91	5.82	2.91	1.82

Table 6: Comparison in terms of FPR95 \downarrow . The **bold**, **purple** and **orange** numbers denote the best, second best, and third best performances, respectively. “Avg. FPR95” and “Avg. Rank” indicates the average FPR95 and rank across all datasets.

Dataset	Graph Kernel + Detector				GNN-based Deep Learning Methods					Proposed Method	
	PK-SVM	PK-iF	WL-SVM	WL-iF	OCGIN	GLocalKD	OCGTL	SIGNET	GLADC	CVTGAD	
MUTAG	88.40 \pm 0.15	86.00 \pm 0.24	78.80 \pm 0.29	86.00 \pm 0.16	45.60 \pm 0.21	48.00 \pm 0.20	39.20\pm0.39	32.00\pm0.24	39.20\pm0.03	38.80 \pm 0.35	30.80\pm0.27
PROTEINS	99.16 \pm 0.23	96.28 \pm 0.21	99.78 \pm 0.25	96.89 \pm 0.22	67.82\pm0.32	76.20 \pm 0.22	94.88 \pm 0.24	84.51 \pm 0.20	71.07\pm0.18	71.16\pm0.30	68.35 \pm 0.30
DD	97.58 \pm 0.20	96.92 \pm 0.19	98.98 \pm 0.22	97.74 \pm 0.21	63.19 \pm 0.32	69.52 \pm 0.19	92.22 \pm 0.21	75.36 \pm 0.18	68.20 \pm 0.17	72.43 \pm 0.20	67.26\pm0.25
ENZYMES	75.08 \pm 0.19	87.57 \pm 0.20	76.40 \pm 0.18	86.80 \pm 0.21	78.93 \pm 0.19	77.42 \pm 0.17	84.97 \pm 0.21	88.10 \pm 0.23	69.35\pm0.32	65.37\pm0.18	60.00 \pm 0.24
DHFR	97.14 \pm 0.19	93.30 \pm 0.18	98.26 \pm 0.21	93.70 \pm 0.19	85.21 \pm 0.20	78.84\pm0.18	94.03 \pm 0.21	73.38\pm0.19	82.76 \pm 0.20	81.73 \pm 0.25	68.95\pm0.23
BZR	92.18 \pm 0.20	94.10 \pm 0.19	92.94 \pm 0.21	93.01 \pm 0.20	72.89\pm0.19	73.92 \pm 0.20	96.65 \pm 0.23	71.54\pm0.29	76.61 \pm 0.21	73.31 \pm 0.20	66.25\pm0.35
COX2	97.83 \pm 0.19	88.61 \pm 0.16	97.05 \pm 0.18	89.29 \pm 0.19	90.07 \pm 0.19	91.04 \pm 0.20	85.12 \pm 0.26	79.14\pm0.30	85.67 \pm 0.23	85.62\pm0.25	78.08\pm0.41
AIDS	98.40 \pm 0.20	58.22 \pm 0.12	99.78 \pm 0.22	58.75 \pm 0.14	13.57 \pm 0.08	14.30 \pm 0.09	1.40\pm0.01	24.98 \pm 0.10	6.79\pm0.05	4.22\pm0.03	6.19 \pm 0.08
IMDB-B	98.61 \pm 0.20	88.32 \pm 0.16	99.60 \pm 0.22	89.80 \pm 0.17	87.89 \pm 0.25	97.83 \pm 0.23	83.21\pm0.18	75.50\pm0.25	77.10 \pm 0.24	75.34\pm0.27	78.05 \pm 0.26
NCII	78.07 \pm 0.25	96.41 \pm 0.21	78.51 \pm 0.22	96.69 \pm 0.23	98.63 \pm 0.23	98.09 \pm 0.22	61.25\pm0.38	80.98 \pm 0.18	96.81 \pm 0.21	85.12\pm0.20	71.84\pm0.33
COLLAB	99.07 \pm 0.20	95.82 \pm 0.18	99.79 \pm 0.23	96.50 \pm 0.20	89.64 \pm 0.19	91.56 \pm 0.20	87.22 \pm 0.21	81.50\pm0.26	81.07\pm0.27	82.35 \pm 0.25	80.15\pm0.28
Avg. FPR95	92.87	89.23	92.72	89.56	72.13	74.25	74.56	70.64	68.60	67.50	61.62
Avg. Rank	8.55	8.05	9.18	8.68	5.45	6.36	5.59	4.55	4.14	3.45	2.00

Our proposed LGKDE demonstrates compelling performance advantages in both precision-recall capabilities and false alarm control. For AUPRC, LGKDE achieves the highest average score of 87.69%, substantially outperforming the second-best method CVTGAD (72.45%). The performance improvement is particularly pronounced on datasets like ENZYMES (97.79% vs. next best 32.67%), MUTAG (96.75% vs. 81.29%), and NCI1 (92.22% vs. 67.45%). On datasets where LGKDE is not the top performer, it still maintains competitive performance with minimal gaps (e.g., BZR: 88.79% vs. best 91.98%; COLLAB: 68.51% vs. best 70.59%). In terms of controlling false positives at high recall rates, LGKDE achieves the lowest average FPR95 of 61.62%, outperforming runner-up approaches CVTGAD (67.50%) and GLADC (68.60%). This represents a significant reduction in false alarms while maintaining high detection rates. LGKDE secures the best FPR95 on 6 out of 11 datasets, with notable improvements on ENZYMES (60.00% vs. next best 65.37%) and DHFR (68.95% vs. next best 73.38%). The consistent superior performance across both metrics is further validated by LGKDE achieving the best average ranks of 1.82 for AUPRC and 2.00 for FPR95, demonstrating its robust detection capabilities across diverse graph structures and domains.

A.4 Additional Validation

This section presents additional experiments to further validate specific aspects of LGKDE, regarding genuine density estimation capabilities and comparisons to two-stage approaches of KDE.

A.4.1 Validation on Synthetic Erdős–Rényi Graphs

To directly assess whether LGKDE learns the underlying probability density function (PDF) of graphs, we performed experiments on synthetically generated Erdős–Rényi (ER) graphs with known generative parameters.

Erdős–Rényi Graph Model. The Erdős–Rényi model $G_{ER}(n, p)$ generates random graphs where each possible edge between n vertices occurs independently with probability $p \in [0, 1]$. Formally, for a graph $G = (V, E, \mathbf{X}) \in \mathbb{G}$ with adjacency matrix \mathbf{A} , each entry \mathbf{A}_{ij} for $i < j$ is an

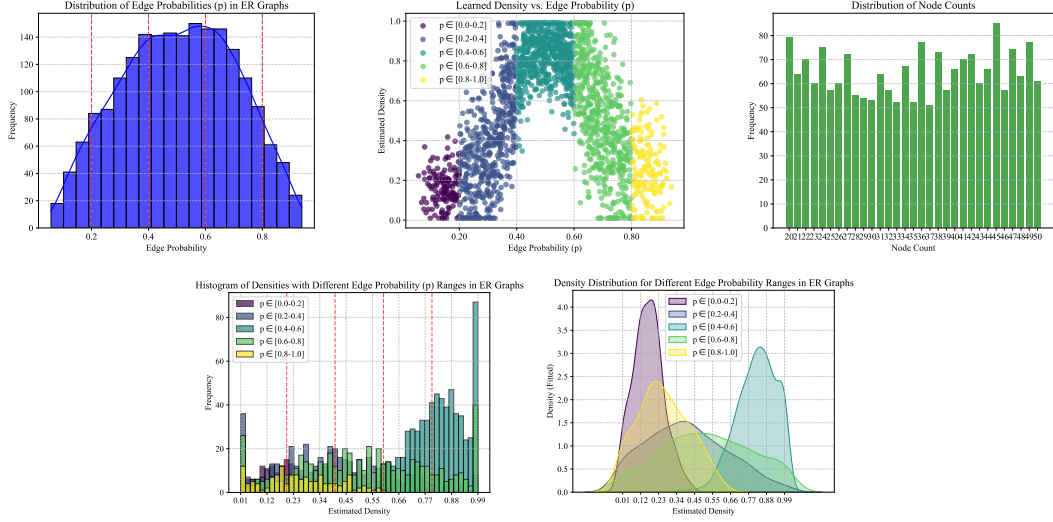


Figure 7: Density estimation results on synthetic Erdős–Rényi graphs. **Row 1 Left:** Ground truth Beta(2, 2) distribution for edge probability p ; **Row 1 Middle:** Learned density estimate from LGKDE versus edge probability p , showing the expected peak around $p = 0.5$; **Row 1 Right:** Distribution of node counts (uniform as generated); **Row 2:** Histogram and Density distributions grouped by edge probability ranges.

independent Bernoulli random variable with parameter p :

$$\mathbf{A}_{ij} = \begin{cases} 1 & \text{with probability } p \\ 0 & \text{with probability } 1 - p \end{cases} \quad \forall i, j \in \{1, 2, \dots, n\}, i < j \quad (14)$$

The resulting graph is undirected with $\mathbf{A}_{ji} = \mathbf{A}_{ij}$ and has no self-loops ($\mathbf{A}_{ii} = 0$). For node features \mathbf{X} , we use the normalized degree of node i .

Experimental Setup. We generated 2000 ER graphs where the number of nodes n was sampled uniformly from $[20, 50]$ and the edge probability p was sampled from a Beta(2, 2) distribution, which peaks at $p = 0.5$. This specific Beta distribution yields a unimodal density that places most probability mass near $p = 0.5$, with decreasing likelihood toward the extremes of $p = 0$ and $p = 1$. LGKDE was trained on this collection of random graphs to test whether it could recover the underlying Beta(2, 2) distribution. If LGKDE accurately estimates the density, it should assign higher density values to graphs whose edge probability p is closer to the mode of the Beta(2, 2) distribution (i.e., $p \approx 0.5$), irrespective of the node count n . Figure 7 and Table 7 present the results.

Table 7: Average estimated density by LGKDE for synthetic ER graphs, grouped by edge probability range.

Edge Probability Range (p)	Average Estimated Density \pm Std Dev
0.0 – 0.2	0.1654 ± 0.0888
0.2 – 0.4	0.3998 ± 0.2428
0.4 – 0.6	0.8222 ± 0.1197
0.6 – 0.8	0.5222 ± 0.2707
0.8 – 1.0	0.2579 ± 0.1522

The results clearly show that LGKDE assigns the highest density to graphs with edge probabilities near 0.5, successfully recovering the underlying generative distribution parameter. This provides strong evidence that LGKDE performs genuine density estimation, not just anomaly boundary learning.

A.4.2 Comparison with Two-Stage Approaches

To evaluate the benefit of LGKDE’s end-to-end learning of the metric and density estimator, we compared it against two-stage approaches on the MUTAG dataset. These approaches first learn graph

embeddings using standard unsupervised graph representation learning methods (InfoGraph [Sun *et al.*, 2019a] and Graph Autoencoder - GAE [Kipf and Welling, 2016]) and then apply a standard multi-bandwidth KDE (using the same bandwidths as LGKDE but with uniform weights) on the learned embeddings.

Table 8: Comparison of LGKDE against two-stage methods (Traditional Methods and Representation Learning + KDE) and traditional baselines on MUTAG.

Method	AUROC (%) \uparrow	AUPRC (%) \uparrow	FPR95 (%) \downarrow
PK-SVM	46.06 \pm 0.47	47.80 \pm 0.25	88.40 \pm 0.15
PK-iF	47.98 \pm 0.41	45.89 \pm 0.21	86.00 \pm 0.24
WL-SVM	62.18 \pm 0.29	50.94 \pm 0.25	78.80 \pm 0.29
WL-iF	65.71 \pm 0.38	55.15 \pm 0.22	86.00 \pm 0.16
InfoGraph+KDE	79.77 \pm 3.05	88.36 \pm 1.53	44.00 \pm 5.66
GAE+KDE	81.94 \pm 2.21	91.00 \pm 1.28	49.60 \pm 5.43
LGKDE (Ours)	91.63 \pm 0.31	96.75 \pm 0.35	30.80 \pm 0.27

Table 8 shows that LGKDE significantly outperforms both two-stage methods of traditional graph kernels + detector and graph representation learning + KDE. While InfoGraph and GAE learn general-purpose embeddings, these are suboptimal for the specific task of density estimation compared to the metric learned jointly within the LGKDE framework. This highlights the advantage of our integrated approach in learning task-relevant representations and distances for accurate density estimation.

A.4.3 Density Gap Analysis under Training Contamination

To quantitatively assess density separation and robustness to label noise, we performed an experiment on MUTAG where we trained LGKDE on the normal class mixed with a varying number of known anomalous samples (treated as normal during training). We then measured the average density assigned by the trained model to the true normal graphs versus the true anomalous graphs (held-out).

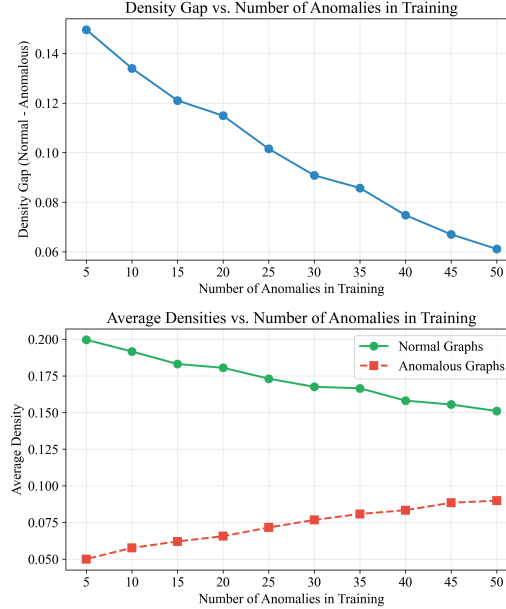


Figure 8: Density gap analysis on MUTAG. Shows the average density assigned to true normal vs. true anomalous graphs when the model is trained with varying numbers of anomalous samples included in the ‘normal’ training set. The gap increases as contamination decreases.

Figure 8 and Table 9 show that even with significant contamination (50 anomalous samples included), LGKDE maintains a positive density gap. As the contamination level decreases, the model learns a better representation of the true normal distribution, resulting in higher density estimates for normal

Table 9: Density gap results on MUTAG under training contamination.

# Anomalies in Training	Avg. Normal Density	Avg. Anomaly Density	Density Gap
50	0.151	0.090	0.061
40	0.158	0.083	0.075
30	0.168	0.077	0.091
20	0.180	0.066	0.115
10	0.192	0.058	0.134
5	0.202	0.053	0.149
0	0.215	0.048	0.167

graphs, lower estimates for anomalous graphs, and a monotonically increasing density gap. This demonstrates both the model’s robustness and its ability to learn a meaningful density separation.

A.4.4 Qualitative Analysis of Learned Densities

To provide qualitative insight into what LGKDE learns, we visualized graphs from the MUTAG dataset corresponding to different density levels estimated by the trained LGKDE model. We identified the "average" graph (minimum mean MMD distance to all others) and samples with the highest and lowest estimated densities.

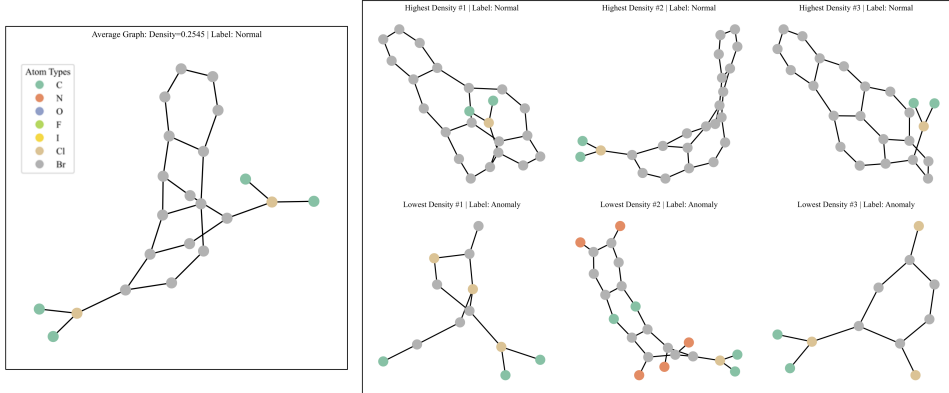


Figure 9: Visualization of MUTAG graphs. (a) The graph with minimum average MMD distance to all other graphs ("average" graph). (b) Top row: examples of graphs assigned the highest density by LGKDE. Bottom row: examples of graphs assigned the lowest density.

Figure 9 reveals structural differences captured by the learned density. High-density (normal) graphs often exhibit more complex ring structures characteristic of the majority class in MUTAG, while low-density (potentially anomalous) graphs tend to have simpler or atypical structures. This visualization supports the idea that LGKDE learns structurally relevant patterns for density estimation.

B Related Work

B.1 Graph Representation Learning

Graph representation learning has emerged as a fundamental paradigm for analyzing graph-structured data [Hamilton, 2020]. Early approaches focused on matrix factorization and random walk-based methods [Perozzi *et al.*, 2014; Grover and Leskovec, 2016], which learn node embeddings by preserving local neighborhood structures. The advent of Graph Neural Networks (GNNs) has revolutionized this field by enabling end-to-end learning of graph representations through message passing [Gilmer *et al.*, 2017]. Modern GNN architectures, such as Graph Convolutional Networks (GCN) [Kipf and Welling, 2017] and Graph Isomorphism Networks (GIN) [Xu *et al.*, 2019], have demonstrated remarkable success in various supervised learning tasks.

However, the challenge of learning effective graph representations without supervision remains significant. Recent unsupervised approaches have explored various strategies, including graph

autoencoders [Kipf and Welling, 2016], contrastive learning [Velickovic *et al.*, 2019], and mutual information maximization [Sun *et al.*, 2019a], graph entropy maximization [Sun *et al.*, 2024]. While these methods have shown promise, they often struggle to capture fine-grained structural patterns and maintain theoretical guarantees, particularly when applied to graph-level representations. Moreover, the lack of supervision makes it especially challenging to learn representations that can effectively distinguish normal patterns from anomalous ones [Ma *et al.*, 2021].

C More Perturbed Sample Generation Details

C.1 Pseudocode of Structure-aware Sample Generation

See Algorithm 1.

C.2 Case Study on Energy-based Spectral Perturbation

Figure 10 and 11 show the visualization of the different combinations of hyperparameters τ_1 and τ_2 in our energy-based spectral perturbation strategy on the first graph from MUTAG datasets. We can find that when τ_1 around 0.5 with τ_2 around 0.75, our method generates structurally meaningful variations (add/remove a suitable number of links in the ring structure) while preserving the graph’s core topology.

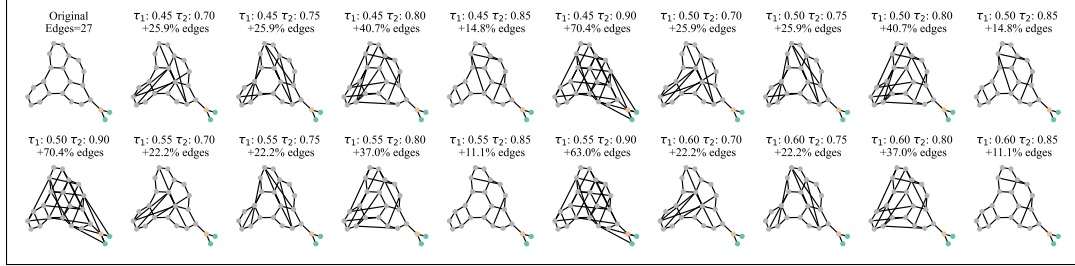


Figure 10: Spectral Perturbation: Add Edges Mode via Amplify \mathcal{S}_l on the 1st MUTAG sample

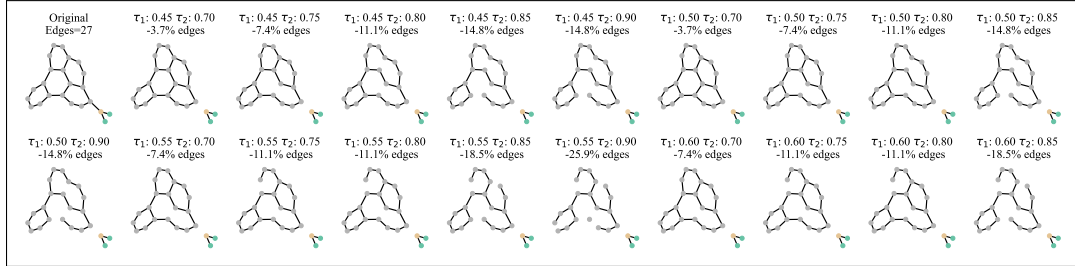


Figure 11: Spectral Perturbation: Remove Edges Mode via Shrink \mathcal{S}_h on the 1st MUTAG sample

Figure 12. shows that the histogram of edge change ratio of spectral perturbation on the whole MUTAG datasets with $\tau_1 = 0.5$ and $\tau_2 = 0.75$, we can find that the majority of graphs have the permutation around add 20% edges or reduce 15% edges. What’s more, these permutation is taken on the graph key structure instead of random edge permutations, which tends to generate well-designed perturbed counterparts and help better characterize the boundary of normal density regions during the unsupervised contrastive learning.

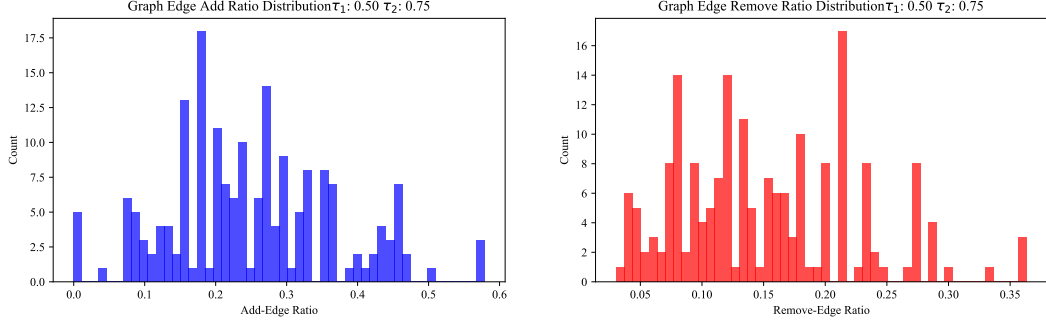


Figure 12: Edge Change Ratio of Spectral Perturbation on the whole MUTAG datasets with $\tau_1 = 0.5$ and $\tau_2 = 0.75$

Algorithm 1 Structure-aware Sample Generation

Require: Graph $G = (\mathbf{A}, \mathbf{X})$, swap ratio r_{swap} , energy thresholds τ_1, τ_2 , edge operation flag $\text{flag} \in \{0, 1\}$ (0: removal, 1: addition)

Ensure: Perturbed graph \tilde{G} with altered structure and features

```

1: function GENERATESAMPLE( $G, r_{\text{swap}}, \tau_1, \tau_2, \text{flag}$ )
2:    $\tilde{\mathbf{X}} \leftarrow \text{NODEFEATUREPERTURB}(\mathbf{X}, r_{\text{swap}})$   $\triangleright$  Swap a fraction of node features
3:    $\tilde{\mathbf{A}} \leftarrow \text{SPECTRALPERTURB}(\mathbf{A}, \tau_1, \tau_2, \text{flag})$   $\triangleright$  Energy-based spectral modification
4:    $\tilde{G} \leftarrow (\tilde{\mathbf{A}}, \tilde{\mathbf{X}})$ 
5:   return  $\tilde{G}$ 
6: end function

7: function NODEFEATUREPERTURB( $\mathbf{X}, r_{\text{swap}}$ )
8:    $\tilde{\mathbf{X}} \leftarrow \mathbf{X}$   $\triangleright$  Initialize copy
9:   Let  $\mathcal{V}_{\text{swap}}$  be a random subset of node indices of size  $\lfloor r_{\text{swap}} \cdot |V| \rfloor$ 
10:   $\tilde{\mathbf{X}}_v \leftarrow \mathbf{X}_{\text{perm}(v)}$  for each  $v \in \mathcal{V}_{\text{swap}}$   $\triangleright$  Shuffle selected nodes' features
11:  return  $\tilde{\mathbf{X}}$ 
12: end function

13: function SPECTRALPERTURB( $\mathbf{A}, \tau_1, \tau_2, \text{flag}$ )
14:    $\mathbf{U}, \Sigma, \mathbf{V}^\top \leftarrow \text{SVD}(\mathbf{A})$   $\triangleright$  SVD decomposition
15:   Compute cumulative energy ratio  $E(k)$  via Eq. (5)
16:   Partition singular values into  $\mathcal{S}_h, \mathcal{S}_m, \mathcal{S}_l$  using thresholds  $\tau_1, \tau_2$ 
17:   Compute adaptive ratio  $r = \min(\mu_h/\mu_l, r_{\text{max}})$ , where  $\mu_h$  and  $\mu_l$  are means of  $\mathcal{S}_h$  and  $\mathcal{S}_l$ 
18:   Modify singular values based on  $\text{flag}$  via Eq. (6):
19:     If  $\text{flag} = 0$  (removal):  $\tilde{\sigma}_i = \sigma_i/r$  for  $\sigma_i \in \mathcal{S}_h$ 
20:     If  $\text{flag} = 1$  (addition):  $\tilde{\sigma}_i = r\sigma_i$  for  $\sigma_i \in \mathcal{S}_l$ 
21:    $\tilde{\Sigma} \leftarrow$  updated diagonal matrix with modified singular values
22:    $\tilde{\mathbf{A}} \leftarrow \mathbf{U} \tilde{\Sigma} \mathbf{V}^\top$ 
23:   return  $\tilde{\mathbf{A}}$ 
24: end function

```

D LGKDE Framework Details

D.1 Multi-scale Kernel Design

The hyperparameter set $\Gamma_{\text{emb}} = \{\gamma_1, \dots, \gamma_S\}$ is chosen to cover multiple scales of the MMD calculation. In practice, we use $S = 5$ and $1/\gamma$ as bandwidths in gaussian kernel k_γ^{emb} , which are logarithmically spaced between γ_{\min} and γ_{\max} . The bandwidth set $H_{\text{KDE}} = \{h_1, \dots, h_M\}$ is used for the multi-scale kernel density estimator. Since they are also Gaussian kernels in MMD calculation and density estimation, and the learnable weights design gives the flexibility to automatically

Algorithm 2 Deep Graph MMD Model for Graph Distance Computation

Require:

- 1: Two sets of graphs $\mathcal{G}_1 = \{G_1^1, \dots, G_1^{N_1}\}$, $\mathcal{G}_2 = \{G_2^1, \dots, G_2^{N_2}\}$ (if $\mathcal{G}_2 = \text{None}$, set $\mathcal{G}_2 \leftarrow \mathcal{G}_1$)
- 2: GNN parameters $\theta = \{\mathbf{W}^{(l)} \in \mathbb{R}^{d_{l-1} \times d_l}\}_{l=1}^L$ for model Φ_θ
- 3: MMD kernel family \mathcal{K}_{emb} with bandwidths $\Gamma_{\text{emb}} = \{\gamma_1, \dots, \gamma_S\}$
- 4: Activation function (ReLU): σ

Ensure: Distance matrix $\mathbf{D} \in \mathbb{R}^{N_1 \times N_2}$ containing pairwise MMD distances

```

5: function COMPUTEMMDDISTANCES( $\mathcal{G}_1, \mathcal{G}_2, \theta, \mathcal{K}_{\text{emb}}$ )
6:   // Generate node embeddings via GNN encoder  $\Phi_\theta$ 
7:   for  $s \in \{1, 2\}$  do
8:     for  $i = 1$  to  $N_s$  do
9:       // Compute  $\mathbf{Z}_s^i = \Phi_\theta(G_s^i)$  with parameters  $\theta$ 
10:      Let  $\mathbf{A}_s^i$  be the adjacency matrix of  $G_s^i$ 
11:      Let  $\mathbf{D}_s^i = \text{diag}(\sum_j \mathbf{A}_s^i[j, :] + 1)$  be the degree matrix with self-loops
12:       $\mathbf{Z}_s^{i,(0)} \leftarrow \mathbf{X}_s^i$                                  $\triangleright$  Initial node features
13:      for  $l = 1$  to  $L$  do
14:         $\hat{\mathbf{A}}_s^i \leftarrow (\mathbf{D}_s^i)^{-1/2}(\mathbf{A}_s^i + \mathbf{I})(\mathbf{D}_s^i)^{-1/2}$            $\triangleright$  Normalized adjacency
15:         $\mathbf{Z}_s^{i,(l)} \leftarrow \sigma(\hat{\mathbf{A}}_s^i \mathbf{Z}_s^{i,(l-1)} \mathbf{W}^{(l)})$            $\triangleright$  GNN layer update
16:      end for
17:       $\mathbf{Z}_s^i \leftarrow \mathbf{Z}_s^{i,(L)}$                                  $\triangleright$  Final node embeddings
18:    end for
19:  end for
20:  // Compute pairwise MMD distances using node embeddings
21:  for  $i = 1$  to  $N_1$  do
22:    for  $j = 1$  to  $N_2$  do
23:      Compute  $\mathbf{D}_{ij} = d_{\text{MMD}}(G_1^i, G_2^j)$  using Eq. (3)
24:      where each kernel evaluation uses Eq. (17) with embeddings  $\mathbf{Z}_1^i$  and  $\mathbf{Z}_2^j$ 
25:    end for
26:  end for
27:  return  $\mathbf{D}$                                  $\triangleright$  Matrix of pairwise MMD distances
28: end function

```

determine the relative kernel importance, we set $M = 5$ and use the same bandwidth in multi-scale KDE H_{KDE} as that in deep MMD calculation. All these designs ensure the kernels can capture both fine-grained local structures and global patterns.

The mixture weights $\{\pi_k\}$ are initialized uniformly and updated through gradient descent on α . The softmax parameterization ensures $\sum_k \pi_k = 1$ while allowing unconstrained optimization of α .

D.2 Optimization Strategy

The complete training and inference procedure of LGKDE is detailed in Algorithm 3. Here we elaborate on key implementation aspects of our optimization approach. The contrastive objective in Eq. (9) can be interpreted as maximizing the difference of densities between normal graphs and their perturbed versions:

$$\min_{\theta, \alpha} \mathcal{L} := - \sum_{i=1}^N \sum_{j=1}^{N_{\text{pert}}} \frac{\hat{f}_{\text{KDE}}(G_i) - \hat{f}_{\text{KDE}}(\tilde{G}_i^{(j)})}{\hat{f}_{\text{KDE}}(G_i) + \epsilon} \quad (15)$$

where $\tilde{G}_i^{(j)}$ denotes the j th perturbed counterpart of G_i and we add ϵ ($\epsilon = 1.0\text{e-}6$ in our experiment) for numerical stability. The objective effectively pushes normal graphs towards high-density regions while moving perturbed versions towards lower-density regions, creating a clear separation in the density landscape.

The parameters θ and α can be optimized jointly using Adam with learning rates η_θ and η_α respectively. We employ gradient clipping and early stopping based on validation set performance to prevent overfitting. The learning rates are scheduled with a warm-up period followed by cosine decay.

Algorithm 3 Learnable Graph Kernel Density Estimation (LGKDE)

Require:

```

1: Normal graph set  $\mathcal{G} = \{G_1, \dots, G_N\}$ 
2: GNN parameters  $\theta$  for encoder  $\Phi_\theta$ , MMD kernel family  $\mathcal{K}_{\text{emb}}$  with bandwidths  $\Gamma_{\text{emb}}$ 
3: Multi-scale KDE bandwidth set  $H_{\text{KDE}} = \{h_k\}_{k=1}^M$ , learnable mixture weight parameters  $\alpha$ 
4: Perturbation parameters:  $N_{\text{pert}}$ ,  $r_{\text{swap}}$ , energy thresholds  $\tau_1, \tau_2$ 
5: Anomaly threshold parameter  $\gamma_{\text{TH}}$  (percentile)

Ensure: Trained model parameters  $\theta, \alpha$ 

6: function TRAIN( $\mathcal{G}$ )
7:   Initialize  $\theta$  and  $\alpha$  randomly
8:   for epoch = 1 to MaxEpoch do
9:     // Generate structure-aware perturbed samples
10:    Sample mini-batch  $\mathcal{B} \subseteq \mathcal{G}$ 
11:    for each graph  $G_i \in \mathcal{B}$  do
12:      for  $j = 1$  to  $N_{\text{pert}}$  do
13:         $flag \leftarrow$  randomly select from  $\{0, 1\}$  ▷ 0: edge removal, 1: edge addition
14:         $\tilde{G}_i^{(j)} \leftarrow \text{GENERATESAMPLE}(G_i, r_{\text{swap}}, \tau_1, \tau_2, flag)$  ▷ Algorithm 1
15:      end for
16:    end for
17:    // Compute MMD distances between all graphs
18:     $\mathbf{D} \leftarrow \text{COMPUTEMMDDISTANCES}(\mathcal{B} \cup \{\tilde{G}_i^{(j)}\}, \mathcal{B}, \theta, \mathcal{K}_{\text{emb}})$  ▷ Algorithm 2
19:    // Compute multi-scale KDE for all graphs
20:    for each graph  $G \in \mathcal{B} \cup \{\tilde{G}_i^{(j)}\}$  do
21:      for  $k = 1$  to  $M$  do
22:         $\phi_k(G) \leftarrow \frac{1}{|\mathcal{B}|} \sum_{G_m \in \mathcal{B}} K_{\text{KDE}}(d_{\text{MMD}}(G, G_m), h_k)$  ▷ k-th KDE component
23:      end for
24:       $\hat{f}_{\text{KDE}}(G) \leftarrow \sum_{k=1}^M \pi_k(\alpha) \phi_k(G)$ , where  $\pi_k(\alpha) = \frac{\exp(\alpha_k)}{\sum_l \exp(\alpha_l)}$ 
25:    end for
26:    // Update parameters using contrastive objective
27:    Compute loss  $\mathcal{L} \leftarrow - \sum_{i=1}^{|\mathcal{B}|} \sum_{j=1}^{N_{\text{pert}}} \frac{\hat{f}_{\text{KDE}}(G_i) - \hat{f}_{\text{KDE}}(\tilde{G}_i^{(j)})}{\hat{f}_{\text{KDE}}(G_i)}$  via Eq. (9)
28:    Update  $\theta, \alpha$  using gradient descent
29:  end for
30:  return  $\theta, \alpha$ 
31: end function

32: function INFERENCE( $G_{\text{test}}$ ,  $\mathcal{G}_{\text{ref}}$ ,  $\theta, \alpha$ )
33:   // Compute density score for test graph
34:    $\mathbf{D} \leftarrow \text{COMPUTEMMDDISTANCES}(\{G_{\text{test}}\}, \mathcal{G}_{\text{ref}}, \theta, \mathcal{K}_{\text{emb}})$  ▷ Algorithm 2
35:   Compute  $\hat{f}_{\text{KDE}}(G_{\text{test}})$  using the multi-scale KDE with parameters  $\alpha$  and distances  $\mathbf{D}$ 
36:    $s(G_{\text{test}}) \leftarrow -\hat{f}_{\text{KDE}}(G_{\text{test}})$  ▷ Convert density to anomaly score
37:   // Compute reference set densities and threshold
38:    $\mathbf{D}_{\text{ref}} \leftarrow \text{COMPUTEMMDDISTANCES}(\mathcal{G}_{\text{ref}}, \mathcal{G}_{\text{ref}}, \theta, \mathcal{K}_{\text{emb}})$ 
39:   Compute  $\hat{f}_{\text{KDE}}(G_i)$  for all  $G_i \in \mathcal{G}_{\text{ref}}$ 
40:    $\tau \leftarrow -\text{Percentile}_{\gamma_{\text{TH}}} \{\hat{f}_{\text{KDE}}(G_i) | G_i \in \mathcal{G}_{\text{ref}}\}$  ▷ Anomaly threshold
41:   return  $s(G_{\text{test}}) > \tau$  ? "Anomalous" : "Normal"
42: end function

```

D.3 Inference Protocol

The percentile-based threshold estimation is robust to outliers and automatically adapts to the scale of density values. In practice, we set $\gamma_{TH} = 10$ as a reasonable default, though this can be adjusted based on domain knowledge about expected anomaly rates.

For computational efficiency during inference, we maintain a reference set of pre-computed node embeddings for normal graphs. This allows fast computation of MMD distances without recomputing embeddings for the reference graphs. The memory requirement scales linearly with the size of the reference set.

E Theoretical Analysis Details

This appendix provides detailed definitions, assumptions, proofs, and technical lemmas supporting all theoretical results presented in Section 4.

E.1 Preliminaries and Definitions

E.1.1 Graph Space and Density

Let \mathbb{G} be the space of attributed graphs $G = (V, E, \mathbf{X})$, represented by (\mathbf{A}, \mathbf{X}) where $\mathbf{A} \in \mathbb{R}^{n \times n}$ ($n = |V|$) is the adjacency matrix and $\mathbf{X} \in \mathbb{R}^{n \times d_{in}}$ is the node feature matrix. We assume graphs are drawn i.i.d. from a probability measure \mathbb{P}^* on \mathbb{G} . We aim to estimate the density f^* of \mathbb{P}^* relative to a base measure μ on \mathbb{G} , such that $\mathbb{P}^*(S) = \int_S f^*(G) d\mu(G)$ for $S \subseteq \mathbb{G}$. The density estimation task is performed within the metric space induced by the learned MMD distance.

E.1.2 GNN Encoder

The L -layer GNN Φ_θ with parameters $\theta = \{\mathbf{W}^{(l)}\}_{l=1}^L$ maps $G = (\mathbf{A}, \mathbf{X})$ to node embeddings $\mathbf{Z} \in \mathbb{R}^{n \times d_{out}}$. A typical layer update (e.g., GCN) is:

$$\mathbf{Z}^{(l)} = \sigma(\hat{\mathbf{A}} \mathbf{Z}^{(l-1)} \mathbf{W}^{(l)}) \quad (16)$$

where $\mathbf{Z}^{(0)} = \mathbf{X} \mathbf{W}^{(0)}$ (or just \mathbf{X} if $d_{in} = d_{hid}$), $\hat{\mathbf{A}}$ is a normalized adjacency matrix (e.g., $\hat{\mathbf{A}} = \mathbf{D}^{-1/2}(\mathbf{A} + \mathbf{I})\mathbf{D}^{-1/2}$), $\mathbf{W}^{(l)} \in \mathbb{R}^{d_{l-1} \times d_l}$, and σ is an activation function. The final output is $\mathbf{Z} = \mathbf{Z}^{(L)}$.

E.1.3 MMD Metric

The squared MMD distance between two graph G_i and G_j (which have their empirical node distributions $P_{\mathbf{Z}_i}$ and $P_{\mathbf{Z}_j}$) using a single kernel $k_\gamma^{\text{emb}}(\cdot, \cdot) \in \mathcal{K}_{\text{emb}}$ is estimated via the biased V-statistic:

$$\hat{d}_{k_\gamma^{\text{emb}}(\cdot, \cdot)}^2(\mathbf{Z}_i, \mathbf{Z}_j) = \frac{1}{n_i^2} \sum_{u, v \in V_i} k_\gamma^{\text{emb}}(\mathbf{z}_u^{(i)}, \mathbf{z}_v^{(i)}; \gamma_s) + \frac{1}{n_j^2} \sum_{u, v \in V_j} k_\gamma^{\text{emb}}(\mathbf{z}_u^{(j)}, \mathbf{z}_v^{(j)}; \gamma_s) - \frac{2}{n_i n_j} \sum_{u \in V_i, v \in V_j} k_\gamma^{\text{emb}}(\mathbf{z}_u^{(i)}, \mathbf{z}_v^{(j)}; \gamma_s) \quad (17)$$

The full metric $d_{\text{MMD}}^2(G_i, G_j) = \sup_{k_\gamma^{\text{emb}}(\cdot, \cdot) \in \mathcal{K}_{\text{emb}}} \hat{d}_{k_\gamma^{\text{emb}}(\cdot, \cdot)}^2(\Phi_\theta(G_i), \Phi_\theta(G_j))$, as shown in paper main content Eq. (3).

E.1.4 Multi-Scale KDE

The estimator is

$$\hat{f}_{\text{KDE}}(G) = \sum_{k=1}^M \pi_k(\boldsymbol{\alpha}) \phi_k(G) = \sum_{k=1}^M \pi_k(\boldsymbol{\alpha}) \frac{1}{N} \sum_{m=1}^N K_{\text{KDE}}(d_{\text{MMD}}(G, G_m), h_k).$$

The kernel $K_{\text{KDE}}(d, h)$ is based on a kernel profile K_0 , e.g., $K_0(t) = e^{-t/2}$ for a Gaussian profile and normalization $C_{d_{\text{int}}} = (2\pi)^{(d_{\text{int}})/2}$. Then, $K_{\text{KDE}}(d, h) = \frac{1}{C_{d_{\text{int}}} h^{d_{\text{int}}}} K_0\left(\frac{d^2}{h^2}\right) = \frac{1}{(2\pi)^{d_{\text{int}}/2} h^{d_{\text{int}}}} e^{-d^2/(2h^2)}$.

E.1.5 Remarks of Assumptions

As given in Section 4, our theoretical analysis of LGKDE framework under the **Assumption 4.1**:

- i) The GNN Φ_θ has bounded weights $\|\mathbf{W}^{(l)}\|_F \leq B_W$.
- ii) The true density f^* is bounded and has bounded second derivatives.

Since using the GCN with ReLU activation function as the backbone of Φ_θ and the Gaussian kernel function of \mathcal{K}_{emb} and K_{KDE} , under **Assumption 4.1**, we can trivially get the following three conditions to further support our analysis:

Condition E.1 (GNN Properties). (i) $\|\mathbf{W}^{(l)}\|_F \leq B_W$; (ii) Activation function σ is ρ_σ -Lipschitz (since ReLU activation function is 1-Lipschitz); (iii) Permutation invariant architecture (nature property for GCN).

Condition E.2 (Density Regularity). (i) $\|f^*\|_\infty \leq M$; (ii) f^* possesses smoothness of order $\beta = 2$, corresponding to bounded second derivatives in the Riemannian manifold induced by the learned MMD metric, interpreted in Remark E.9.

Condition E.3 (Kernel Properties). MMD kernels \mathcal{K}_{emb} are characteristic. KDE kernel profile is symmetric, non-negative, and has sufficient smoothness (since both kernel types are typically Gaussian, they have infinite order of smoothness).

E.2 Proof of Theorem 4.2 (Consistency)

Proof. The proof relies on showing that both the bias and variance of the estimator \hat{f}_{KDE} converge to zero under the given conditions. We analyze the estimator assuming optimal fixed parameters θ^*, α^* . Let $d^*(G, G') = d_{\text{MMD}}|_{\theta=\theta^*}(G, G')$ denote the MMD metric with these optimal parameters.

1. Bias Analysis: The expected value of the estimator is:

$$\begin{aligned}\mathbb{E}[\hat{f}_{\text{KDE}}(G)] &= \mathbb{E}\left[\sum_{k=1}^M \pi_k^* \frac{1}{N} \sum_{m=1}^N K_{\text{KDE}}(d^*(G, G_m), h_k)\right] \\ &= \sum_{k=1}^M \pi_k^* \mathbb{E}_{G' \sim \mathbb{P}^*}[K_{\text{KDE}}(d^*(G, G'), h_k)] \\ &= \sum_{k=1}^M \pi_k^* \int_{\mathbb{G}} K_{\text{KDE}}(d^*(G, G'), h_k) f^*(G') d\mu(G')\end{aligned}$$

Let $K_h(G, G') = K_{\text{KDE}}(d^*(G, G'), h)$. This is a kernel function defined on the graph space \mathbb{G} using the metric d^* .

Under the Assumption 4.1: **ii**) f^* is bounded and has bounded second derivatives ($\beta = 2$ smoothness) and the kernel K_{KDE} satisfies standard moment conditions (e.g., symmetric profile K_0), we can apply a Taylor expansion of $f^*(G')$ around G . In the metric space (\mathbb{G}, d^*) , this expansion can be written as:

$$f^*(G') = f^*(G) + \nabla f^*(G) \cdot \text{expmap}_G^{-1}(G') + \frac{1}{2} \nabla^2 f^*(G) [\text{expmap}_G^{-1}(G'), \text{expmap}_G^{-1}(G')] + o(d^*(G, G')^2)$$

where ∇f^* is the gradient, $\nabla^2 f^*$ is the Hessian operator in the Riemannian manifold \mathcal{M} induced by d^* , and $\text{expmap}_G^{-1}(G')$ is the inverse exponential map that maps G' to a tangent vector at G (See Remark E.9). Under the symmetry conditions of the kernel and using properties of Riemannian geometry, this leads to:

$$\int K_h(G, G') f^*(G') d\mu(G') = f^*(G) \int K_h(G, G') d\mu(G') + \frac{h^2}{2} \mu_2(K_0) \Delta_{d^*} f^*(G) + o(h^2)$$

where $\int K_h(G, G') d\mu(G') \rightarrow 1$ as $h \rightarrow 0$, μ_2 is the second moment of the kernel profile, and $\Delta_{d^*} f^*(G)$ represents the Laplace-Beltrami operator (the trace of the Hessian) applied to f^* at point G in the Riemannian manifold induced by the metric d^* .

Thus, the bias is:

$$\text{Bias}(\hat{f}_{\text{KDE}}(G)) = \mathbb{E}[\hat{f}_{\text{KDE}}(G)] - f^*(G) = \sum_{k=1}^M \pi_k^* \left(\frac{h_k^2}{2} \mu_2(K_0) \Delta_{d^*} f^*(G) + o(h_k^2) \right)$$

As $h_k \rightarrow 0$, the bias converges to 0 pointwise.

2. Variance Analysis:

$$\begin{aligned}\text{Var}(\hat{f}_{KDE}(G)) &= \text{Var}\left(\sum_{k=1}^M \pi_k^* \frac{1}{N} \sum_{m=1}^N K_{h_k}(G, G_m)\right) \\ &= \text{Var}\left(\frac{1}{N} \sum_{m=1}^N \left[\sum_{k=1}^M \pi_k^* K_{h_k}(G, G_m) \right]\right) \quad (\text{rearranging terms})\end{aligned}$$

Since G_1, G_2, \dots, G_N are i.i.d. samples from \mathbb{P}^* , the kernel evaluations $K_{h_k}(G, G_m)$ for a fixed test point G are also i.i.d. random variables. Using the property that for i.i.d. random variables X_1, \dots, X_N with common variance σ^2 , we have $\text{Var}(\frac{1}{N} \sum_{i=1}^N X_i) = \frac{\sigma^2}{N}$, we obtain:

$$\begin{aligned}\text{Var}(\hat{f}_{KDE}(G)) &= \frac{1}{N} \text{Var}\left(\sum_{k=1}^M \pi_k^* K_{h_k}(G, G_1)\right) \\ &\leq \frac{1}{N} \mathbb{E}\left[\left(\sum_{k=1}^M \pi_k^* K_{h_k}(G, G_1)\right)^2\right] \quad (\text{since } \text{Var}(X) \leq \mathbb{E}[X^2]) \\ &= \frac{1}{N} \mathbb{E}\left[\sum_{k=1}^M \sum_{j=1}^M \pi_k^* \pi_j^* K_{h_k}(G, G_1) K_{h_j}(G, G_1)\right] \\ &= \frac{1}{N} \sum_{k=1}^M \sum_{j=1}^M \pi_k^* \pi_j^* \mathbb{E}[K_{h_k}(G, G_1) K_{h_j}(G, G_1)]\end{aligned}$$

For small bandwidths, $K_h(G, G')$ is concentrated around $G' = G$.

$$\mathbb{E}[K_h(G, G_1)^2] = \int K_h(G, G')^2 f^*(G') d\mu(G') \approx f^*(G) \int K_h(G, G')^2 d\mu(G')$$

Using the definition $K_h(G, G') = \frac{1}{C_{d_{\text{int}}} h^{d_{\text{int}}}} K_0\left(\frac{d^*(G, G')^2}{h^2}\right)$, we have $\int K_h(G, G')^2 d\mu(G') \approx \frac{R(K_0)}{h^{d_{\text{int}}}}$, where $R(K_0) = \frac{\int K_0(t)^2 dt}{C_{d_{\text{int}}}}$.

So, $\text{Var}(\phi_j(G)) \approx \frac{f^*(G)R(K_0)}{N h_k^{d_{\text{int}}}}$. The variance of the sum is bounded by:

$$\text{Var}(\hat{f}_{KDE}(G)) \leq \frac{C}{N} \sum_{k,j} \pi_k^* \pi_j^* \frac{1}{(\min(h_k, h_j))^{d_{\text{int}}}} = O\left(\frac{1}{N(\min_k h_k)^{d_{\text{int}}}}\right)$$

More accurately, $\text{Var}(\hat{f}_{KDE}(G)) \approx \frac{f^*(G)}{N} \sum_{k,j} \pi_k^* \pi_j^* \int K_{h_k}(G, G') K_{h_j}(G, G') d\mu(G')$. For diagonal terms ($k = j$), this gives the $1/(Nh_k^{d_{\text{int}}})$ scaling. Off-diagonal terms are typically smaller. The overall rate is dominated by the smallest bandwidth if weights are comparable. As $Nh_k^{d_{\text{int}}} \rightarrow \infty$ for all k , the variance converges to 0 pointwise.

3. L_1 Convergence: $\mathbb{E} \int |\hat{f}_{KDE}(G) - f^*(G)| d\mathbb{P}^*(G) = \int \mathbb{E}[|\hat{f}_{KDE}(G) - f^*(G)|] d\mathbb{P}^*(G)$. Since $\mathbb{E}[|\cdot|] \leq \sqrt{\mathbb{E}[(\cdot)^2]} = \sqrt{\text{Bias}^2 + \text{Var}}$, and both bias and variance integrate to 0 (assuming uniform bounds or using dominated convergence), the expected L_1 error converges to 0. Convergence in probability follows. \square

E.3 Proof of Theorem 4.3 (Convergence Rate)

Proof. The MISE is $\int (\text{Bias}^2(G) + \text{Var}(G))d\mu(G)$. Using the bias and variance approximations from Appendix E.2, we can get the integrated squared bias (ISB),

$$\begin{aligned} \text{ISB} &= \int \left(\sum_{k=1}^M \pi_k^* \frac{h_k^2}{2} \mu_2 \Delta_{d^*} f^*(G) + o(\sum \pi_k^* h_k^2) \right)^2 d\mu(G) \\ &\approx \left(\sum_{k=1}^M \pi_k^* \frac{h_k^2}{2} \mu_2 \right)^2 \int (\Delta_{d^*} f^*(G))^2 d\mu(G) = O((\sum \pi_k^* h_k^2)^2) = O(h_{avg}^4) \end{aligned}$$

where $h_{avg}^2 = \sum_k \pi_k^* h_k^2$ represents the effective squared bandwidth as a weighted average of individual bandwidths. And the integrated variance (IV),

$$\begin{aligned} \text{IV} &= \int \frac{1}{N} \sum_{k,j} \pi_k^* \pi_j^* \mathbb{E}[K_{h_k}(G, G_1) K_{h_j}(G, G_1)] d\mu(G) \\ &\approx \frac{1}{N} \sum_k (\pi_k^*)^2 \int \frac{f^*(G) R(K_0)}{h_k^{d_{\text{int}}}} d\mu(G) \quad (\text{ignoring off-diagonal terms}) \\ &= O\left(\frac{1}{N} \sum_k \frac{(\pi_k^*)^2}{h_k^{d_{\text{int}}}}\right) \end{aligned}$$

Now we finally get that $\text{MISE} \approx A \cdot h_{avg}^4 + B \cdot \frac{1}{N} \sum_k \frac{(\pi_k^*)^2}{h_k^{d_{\text{int}}}}$.

If we consider a single effective bandwidth h , $\text{MISE} \approx Ah^4 + B'/(Nh^{d_{\text{int}}})$. Minimizing w.r.t h gives $h^* \sim N^{-1/(4+d_{\text{int}})}$ and $\text{MISE} \sim N^{-4/(4+d_{\text{int}})}$. What's more, since we are utilizing the pairwise MMD distance for our LGKDE, MISE is bounded to $O(N^{-0.8})$ for $d_{\text{int}} = 1$, demonstrating the statistical efficiency of our approach. \square

E.4 Proof of Robustness

E.4.1 Proof of Theorem E.4 (Robustness of KDE to Metric Perturbations)

Theorem E.4 (Robustness of KDE to Metric Perturbations). *Under Assumption 4.1 (Condition E.1 and E.3 hold), and the KDE kernel $K_{\text{KDE}}(d, h)$ is twice differentiable w.r.t. d . For fixed parameters θ, α , and any two graphs $G_1, G_2 \in \mathbb{G}$ such that $d_{12} = d_{\text{MMD}}|_{\theta}(G_1, G_2)$ is sufficiently small:*

$$|\hat{f}_{\text{KDE}}(G_1) - \hat{f}_{\text{KDE}}(G_2)| \leq L_{\text{KDE}} \cdot d_{12} + C_{\text{KDE}} \cdot d_{12}^2 + o(d_{12}^2) \quad (18)$$

where the Lipschitz constant L_{KDE} and the second-order coefficient C_{KDE} are given by:

$$\begin{aligned} L_{\text{KDE}} &= \sum_{k=1}^M \pi_k(\alpha) \mathbb{E}_{G_m \sim \mathbb{P}^*} \left[\left| \frac{\partial K_{\text{KDE}}}{\partial d}(d_{\text{MMD}}|_{\theta}(G_1, G_m), h_k) \right| \right] \\ C_{\text{KDE}} &= \frac{1}{2} \sum_{k=1}^M \pi_k(\alpha) \mathbb{E}_{G_m \sim \mathbb{P}^*} \left[\sup_{d' \in [d_{\text{MMD}}|_{\theta}(G_1, G_m), d_{\text{MMD}}|_{\theta}(G_2, G_m)]} \left| \frac{\partial^2 K_{\text{KDE}}}{\partial d^2}(d', h_k) \right| \right] \end{aligned} \quad (19)$$

The constants depend on the KDE kernel derivatives (bounded under Condition E.3), bandwidths H_{KDE} , weights $\pi_k(\alpha)$, the GNN parameters θ , and the distribution \mathbb{P}^* via the expectation over reference graphs G_m . For Gaussian KDE kernels,

$$L_{\text{KDE}} = O(\sum_k \pi_k / h_k^{d_{\text{int}}+1}) = O\left(\frac{1}{h_{\min}}\right) \text{ and } C_{\text{KDE}} = O(\sum_k \pi_k / h_k^{d_{\text{int}}+2}) = O\left(\frac{1}{h_{\min}^3}\right).$$

Proof. Let $G_1, G_2 \in \mathbb{G}$. The MMD distance between them under the fixed GNN parameters θ is $d_{12} = d_{\text{MMD}}(G_1, G_2)$. For any reference graph $G_m \sim \mathbb{P}^*$, let $d_{1m} = d_{\text{MMD}}(G_1, G_m)$ and $d_{2m} = d_{\text{MMD}}(G_2, G_m)$. By the triangle inequality for the metric d_{MMD} (which holds for fixed θ), we have:

$$|d_{1m} - d_{2m}| \leq d_{\text{MMD}}(G_1, G_2) = d_{12}.$$

The KDE estimate for an arbitrary graph G is given by:

$$\hat{f}_{KDE}(G) = \sum_{k=1}^M \pi_k(\boldsymbol{\alpha}) \frac{1}{N} \sum_{j=1}^N K_{KDE}(d_{MMD}(G, G_j), h_k)$$

where $\{G_j\}_{j=1}^N$ is a reference set of N graphs, typically sampled from \mathbb{P}^* . The difference in KDE estimates for G_1 and G_2 is:

$$\begin{aligned} |\hat{f}_{KDE}(G_1) - \hat{f}_{KDE}(G_2)| &= \left| \sum_{k=1}^M \pi_k(\boldsymbol{\alpha}) \frac{1}{N} \sum_{j=1}^N [K_{KDE}(d_{MMD}(G_1, G_j), h_k) - K_{KDE}(d_{MMD}(G_2, G_j), h_k)] \right| \\ &\leq \sum_{k=1}^M \pi_k(\boldsymbol{\alpha}) \frac{1}{N} \sum_{j=1}^N |K_{KDE}(d_{1j}, h_k) - K_{KDE}(d_{2j}, h_k)| \end{aligned}$$

where $d_{1j} = d_{MMD}(G_1, G_j)$ and $d_{2j} = d_{MMD}(G_2, G_j)$. As $N \rightarrow \infty$, the empirical average $\frac{1}{N} \sum_{j=1}^N (\cdot)$ converges to the expectation $\mathbb{E}_{G_m \sim \mathbb{P}^*}[(\cdot)]$. Thus, we analyze the properties based on this expectation.

Consider a single KDE component k and a reference graph $G_m \sim \mathbb{P}^*$. Let $f_k(d) = K_{KDE}(d, h_k)$. Since K_{KDE} is twice differentiable with respect to d , we perform a second-order Taylor expansion of $f_k(d_{2m})$ around d_{1m} . Let $\delta_m = d_{2m} - d_{1m}$. We know from the triangle inequality that $|\delta_m| \leq d_{12}$.

$$f_k(d_{2m}) = f_k(d_{1m} + \delta_m) = f_k(d_{1m}) + \frac{\partial f_k}{\partial d}(d_{1m})\delta_m + \frac{1}{2} \frac{\partial^2 f_k}{\partial d^2}(\xi_{m,k})\delta_m^2$$

where $\xi_{m,k}$ is some value between d_{1m} and d_{2m} . Therefore,

$$\begin{aligned} |f_k(d_{1m}) - f_k(d_{2m})| &\leq \left| \frac{\partial K_{KDE}}{\partial d}(d_{1m}, h_k) \right| |\delta_m| + \frac{1}{2} \left| \frac{\partial^2 K_{KDE}}{\partial d^2}(\xi_{m,k}, h_k) \right| \delta_m^2 \\ &\leq \left| \frac{\partial K_{KDE}}{\partial d}(d_{1m}, h_k) \right| d_{12} + \frac{1}{2} \sup_{d' \in [\min(d_{1m}, d_{2m}), \max(d_{1m}, d_{2m})]} \left| \frac{\partial^2 K_{KDE}}{\partial d^2}(d', h_k) \right| d_{12}^2 \end{aligned}$$

Taking the expectation $\mathbb{E}_{G_m \sim \mathbb{P}^*}$ (which is what the sum over N reference samples approximates) and summing over the KDE components $k = 1, \dots, M$ weighted by $\pi_k(\boldsymbol{\alpha})$:

$$\begin{aligned} |\hat{f}_{KDE}(G_1) - \hat{f}_{KDE}(G_2)| &\leq \mathbb{E}_{G_m \sim \mathbb{P}^*} \left[\sum_{k=1}^M \pi_k(\boldsymbol{\alpha}) |K_{KDE}(d_{1m}, h_k) - K_{KDE}(d_{2m}, h_k)| \right] + o(d_{12}^2) \\ &\leq \sum_{k=1}^M \pi_k(\boldsymbol{\alpha}) \mathbb{E}_{G_m \sim \mathbb{P}^*} \left[\left| \frac{\partial K_{KDE}}{\partial d}(d_{1m}, h_k) \right| \right] d_{12} \\ &\quad + \frac{1}{2} \sum_{k=1}^M \pi_k(\boldsymbol{\alpha}) \mathbb{E}_{G_m \sim \mathbb{P}^*} \left[\sup_{d' \in [\min(d_{1m}, d_{2m}), \max(d_{1m}, d_{2m})]} \left| \frac{\partial^2 K_{KDE}}{\partial d^2}(d', h_k) \right| \right] d_{12}^2 + o(d_{12}^2) \end{aligned}$$

We can now identify the terms L_{KDE} and C_{KDE} from the theorem statement:

$$\begin{aligned} L_{KDE} &= \sum_{k=1}^M \pi_k(\boldsymbol{\alpha}) \mathbb{E}_{G_m \sim \mathbb{P}^*} \left[\left| \frac{\partial K_{KDE}}{\partial d}(d_{MMD}(G_1, G_m), h_k) \right| \right] \\ C_{KDE} &= \frac{1}{2} \sum_{k=1}^M \pi_k(\boldsymbol{\alpha}) \mathbb{E}_{G_m \sim \mathbb{P}^*} \left[\sup_{d' \in [d_{MMD}(G_1, G_m), d_{MMD}(G_2, G_m)]} \left| \frac{\partial^2 K_{KDE}}{\partial d^2}(d', h_k) \right| \right] \end{aligned}$$

Now we start the order analysis for Gaussian KDE kernels:

For a Gaussian KDE kernel $K_{KDE}(d, h) = \frac{1}{(2\pi)^{d_{int}/2} h^{d_{int}}} e^{-d^2/(2h^2)}$, the first derivative $\frac{\partial K_{KDE}}{\partial d} = -\frac{d}{h^2} K_{KDE}(d, h)$. Its magnitude is $O(1/h^{d_{int}+1})$. Thus, $L_{KDE} = O(\sum_k \pi_k / h_k^{d_{int}+1})$.

The second derivative $\frac{\partial^2 K_{KDE}}{\partial d^2} = (\frac{d^2}{h^4} - \frac{1}{h^2}) K_{KDE}(d, h)$, which is $O(1/h^{d_{int}+2})$. Thus, $C_{KDE} = O(\sum_k \pi_k / h_k^{d_{int}+2})$.

The maximum magnitude of this derivative occurs at $d = h$, where it equals $\frac{1}{h\sqrt{e}}$. With bandwidth range $h_{min} \leq h_k \leq h_{max}$ and normalized weights $\sum_{k=1}^M \pi_k = 1$:

$$L_{KDE} = \sum_{k=1}^M \pi_k(\boldsymbol{\alpha}) \mathbb{E}_{G_m \sim \mathbb{P}^*} \left[\left| \frac{\partial K_{KDE}}{\partial d}(d_{1m}, h_k) \right| \right] \leq \frac{1}{h_{min}\sqrt{e}} \quad (20)$$

Similarly, for the second derivative: $\frac{\partial^2 K_{KDE}}{\partial d^2} = \left(\frac{d^2}{h^4} - \frac{1}{h^2} \right) K_{KDE}(d, h)$, the maximum magnitude occurs near $d = \sqrt{3}h$, giving:

$$C_{KDE} = \frac{1}{2} \sum_{k=1}^M \pi_k(\boldsymbol{\alpha}) \mathbb{E}_{G_m \sim \mathbb{P}^*} \left[\sup_{d'} \left| \frac{\partial^2 K_{KDE}}{\partial d^2}(d', h_k) \right| \right] \leq \frac{C_2}{2h_{min}^3} \quad (21)$$

where C_2 is a constant that depends on the specific Gaussian profile.

In asymptotic notation, for our multi-scale Gaussian KDE with minimum bandwidth $h_{min} \in H_{KDE}$, we can finally get:

$$L_{KDE} = O\left(\frac{1}{h_{min}}\right), \quad C_{KDE} = O\left(\frac{1}{h_{min}^3}\right) \quad (22)$$

This completes the proof. \square

E.4.2 Proof of Proposition E.5 (Robustness of MMD to Graph Perturbations)

Proposition E.5 (Robustness of MMD to Graph Perturbations). *Under Condition E.1 and E.3, let $\tilde{G} = (\tilde{\mathbf{A}}, \tilde{\mathbf{X}})$ be perturbed from $G = (\mathbf{A}, \mathbf{X})$ with $\|\mathbf{X}\|_F \leq B_X$, $\|\Delta\mathbf{X}\|_F \leq B_{\Delta X}$ and $\|\hat{\mathbf{A}} - \tilde{\mathbf{A}}\|_F \leq B_{\Delta \hat{\mathbf{A}}}$. Then:*

$$d_{MMD}(G, \tilde{G}) \leq \Delta_{perturb} \quad (23)$$

where $\Delta_{perturb}$ explicitly bounds the maximum MMD distance induced by the perturbation, defined as:

$$\Delta_{perturb} = \frac{L_\mu^*}{\sqrt{n}} (\rho_\sigma B_W)^L (B_{\Delta X} + L \cdot B_X \cdot B_{\Delta \hat{\mathbf{A}}}) \quad (24)$$

where

- n is the graph node size, L is the layer number of Φ_θ .
- $L_\mu^* = \sup_{k \in \mathcal{K}_{emb}} L_\mu(k)$ as Lipschitz constant of mean map, where k denotes a kernel function from the family \mathcal{K}_{emb} .
- ρ_σ is the Lipschitz constant of the GNN activation function.
- B_W is the GNN weight norm bound.
- $B_{\Delta \hat{\mathbf{A}}} = O(n^{3/2} d_{min}^{-2} \|\Delta \mathbf{A}\|_F)$, where $\|\Delta \mathbf{A}\|_F = \|\tilde{\Sigma} - \Sigma\|_F \leq \sqrt{p_{pert} n} \cdot \sigma_{max} \cdot \max(|r-1|, |1/r-1|)$, p_{pert} is the fraction of singular values be modified by with ratio r . It bounds the change in the normalized adjacency matrix due to spectral perturbations (see proof and analysis in Lemma E.16).
- $B_{\Delta X} \leq 2B_x \sqrt{r_{swap} \cdot n}$ gives the bound for feature perturbations and depends on feature swap ratio r_{swap} and feature bound B_x .

More specifically, we using ReLU activation functions, $\rho_\sigma = 1$ since ReLU is 1-Lipschitz. And $L_\mu^* = O(\sqrt{\gamma_{max}})$ for Gaussian kernel family with $\gamma \in \Gamma_{emb} = \{\gamma_1, \dots, \gamma_S\}$. We can get the bound to:

$$\begin{aligned} \Delta_{perturb} &= \frac{L_\mu^*}{\sqrt{n}} (B_W)^L (B_{\Delta X} + L \cdot B_X \cdot B_{\Delta \hat{\mathbf{A}}}) \\ &= O\left(\sqrt{\gamma_{max}} \cdot (B_W)^L \cdot \left(\sqrt{r_{swap}} + \frac{n \cdot \sqrt{p_{pert}} \cdot \sigma_{max} \cdot \max(|r-1|, |1/r-1|)}{d_{min}^2}\right)\right) \end{aligned} \quad (25)$$

Proof. Let $G = (\mathbf{A}, \mathbf{X})$ and its perturbed version be $\tilde{G} = (\tilde{\mathbf{A}}, \tilde{\mathbf{X}})$. Both graphs have n nodes. The GNN encoder Φ_θ operates with fixed parameters θ . Let $\mathbf{Z} = \Phi_\theta(G)$ and $\tilde{\mathbf{Z}} = \Phi_\theta(\tilde{G})$ be their

respective node embeddings. The MMD distance is $d_{MMD}|\theta(G, \tilde{G})$. The proof involves two main steps:

Step 1: Bound the perturbation in node embeddings $\|\Delta \mathbf{Z}\|_F = \|\tilde{\mathbf{Z}} - \mathbf{Z}\|_F$. Let $\Delta \mathbf{X} = \tilde{\mathbf{X}} - \mathbf{X}$ and $\Delta \hat{\mathbf{A}} = \hat{\mathbf{A}} - \tilde{\mathbf{A}}$, where $\hat{\mathbf{A}}$ and $\tilde{\mathbf{A}}$ are the normalized adjacency matrices for G and \tilde{G} . The proposition states bounds B_X for $\|\mathbf{X}\|_F$, $B_{\Delta X}$ for $\|\Delta \mathbf{X}\|_F$, and $B_{\Delta \hat{\mathbf{A}}}$ for $\|\hat{\mathbf{A}} - \tilde{\mathbf{A}}\|_F$. Under Condition E.1 (which includes bounds B_W on GNN weight norms $\|\mathbf{W}^{(l)}\|_F$, and ρ_σ for the activation Lipschitz constant), Lemma E.12 establishes the following bound on the difference in the final L -layer embeddings:

$$\|\Delta \mathbf{Z}\|_F \leq (\rho_\sigma B_W)^L \|\Delta \mathbf{X}\|_F + \|\hat{\mathbf{A}} - \tilde{\mathbf{A}}\|_F L (\rho_\sigma B_W)^L \|\mathbf{X}\|_F$$

Using the assumed bounds from the proposition statement:

$$\|\Delta \mathbf{Z}\|_F \leq (\rho_\sigma B_W)^L (B_{\Delta X} + L \cdot B_X \cdot B_{\Delta \hat{\mathbf{A}}}) \quad (26)$$

The proposition further details that $B_{\Delta X} \leq 2B_x \sqrt{r_{swap} \cdot n}$ based on per-node feature bounds B_x and swap ratio r_{swap} , and $B_{\Delta \hat{\mathbf{A}}}$ (related to changes in the normalized adjacency matrix) is elaborated in Lemma E.16.

Step 2: Bound the MMD distance $d_{MMD}|\theta(G, \tilde{G})$. Let $P_{\mathbf{Z}} = \frac{1}{n} \sum_{v=1}^n \delta_{\mathbf{z}_v}$ and $P_{\tilde{\mathbf{Z}}} = \frac{1}{n} \sum_{v=1}^n \delta_{\tilde{\mathbf{z}}_v}$ be the empirical distributions of node embeddings generated by Φ_θ (with fixed parameters θ). Let $L_\mu^* = \sup_{k \in \mathcal{K}_{emb}} L_\mu(k)$, where $L_\mu(k)$ is the Lipschitz constant of the kernel mean embedding map for $k \in \mathcal{K}_{emb}$ (Condition E.3). From Lemma E.17 (MMD Stability), the MMD distance $d_{MMD}|\theta(G, \tilde{G})$ (which is $\sup_{k \in \mathcal{K}_{emb}} d_k(P_{\mathbf{Z}}, P_{\tilde{\mathbf{Z}}})$) is bounded by:

$$d_{MMD}|\theta(G, \tilde{G}) \leq L_\mu^* \frac{\|\Delta \mathbf{Z}\|_F}{\sqrt{n}}$$

Substituting the bound for $\|\Delta \mathbf{Z}\|_F$ from Eq. (26):

$$d_{MMD}|\theta(G, \tilde{G}) \leq \frac{L_\mu^*}{\sqrt{n}} ((\rho_\sigma B_W)^L (B_{\Delta X} + L \cdot B_X \cdot B_{\Delta \hat{\mathbf{A}}})) = \Delta_{perturb}$$

More specifically, we use ReLU activation functions, $\rho_\sigma = 1$ since ReLU is 1-Lipschitz. $L_\mu^* = \sup_{\gamma \in \Gamma_{emb}} L_\mu(k_{emb}^\gamma) = O(\sqrt{\gamma_{max}})$ since Gaussian kernel family $k_{emb}^\gamma(\mathbf{u}, \mathbf{v}) = \exp(-\gamma_s \|\mathbf{u} - \mathbf{v}\|^2)$ with $\gamma \in \Gamma_{emb} = \{\gamma_1, \dots, \gamma_S\}$ and $L_\mu(k_{emb}^\gamma) = O(\sqrt{\gamma})$.

Substituting all available terms and we can get the bound to $\Delta_{perturb}$ as defined in Equation (12) of Proposition E.5:

$$\Delta_{perturb} = O \left(\sqrt{\gamma_{max}} \cdot (B_W)^L \cdot \left(\sqrt{r_{swap}} + \frac{n \cdot \sqrt{p_{pert}} \cdot \sigma_{max} \cdot \max(|r-1|, |1/r-1|)}{d_{min}^2} \right) \right)$$

This completes the proof. \square

E.4.3 Proof of Corollary E.6 (Robustness of KDE to Graph Perturbations)

Corollary E.6 (Robustness of KDE to Graph Perturbations). *Under the conditions of Theorem E.4 and Proposition E.5:*

$$|\hat{f}_{KDE}(G) - \hat{f}_{KDE}(\tilde{G})| \leq L_{KDE} \cdot \Delta_{perturb} + C_{KDE} \cdot \Delta_{perturb}^2 + o(\Delta_{perturb}^2) \quad (27)$$

where L_{KDE} , C_{KDE} , and $\Delta_{perturb}$ are defined in the respective theorems/propositions above.

Proof. This corollary combines the results from Theorem E.4 and Proposition E.5. Theorem E.4 states that for any two graphs $G_1, G_2 \in \mathbb{G}$, and their MMD distance $d_{12} = d_{MMD}|\theta(G_1, G_2)$ computed under fixed GNN parameters θ :

$$\begin{aligned} |\hat{f}_{KDE}(G_1) - \hat{f}_{KDE}(G_2)| &\leq L_{KDE} \cdot d_{12} + C_{KDE} \cdot d_{12}^2 + o(d_{12}^2) \\ &= O(h_{min}^{-1} \Delta_{perturb} + h_{min}^{-3} \Delta_{perturb}^2) \end{aligned}$$

The constants L_{KDE} and C_{KDE} are also defined under these fixed θ and α , as detailed in Theorem E.4.

Proposition E.5 provides an upper bound for the MMD distance between an original graph G and its perturbed version \tilde{G} , under the same fixed GNN parameters θ :

$$d_{MMD}|\theta(G, \tilde{G}) \leq \Delta_{perturb}$$

where

$$\Delta_{perturb} = O\left(\sqrt{\gamma_{max}} \cdot (B_W)^L \cdot \left(\sqrt{r_{swap}} + \frac{n \cdot \sqrt{p_{pert}} \cdot \sigma_{max} \cdot \max(|r-1|, |1/r-1|)}{d_{min}^2}\right)\right).$$

To obtain the bound for $|\hat{f}_{KDE}(G) - \hat{f}_{KDE}(\tilde{G})|$, we apply Theorem E.4 by setting $G_1 = G$ and $G_2 = \tilde{G}$. The distance term d_{12} becomes $d_{MMD}|\theta(G, \tilde{G})$. From Proposition E.5, we know that $d_{MMD}|\theta(G, \tilde{G}) \leq \Delta_{perturb}$. Since $L_{KDE} \geq 0$ and $C_{KDE} \geq 0$ (as they involve sums of absolute values or supremum of absolute values of kernel derivatives, and non-negative mixture weights π_k), the terms $L_{KDE} \cdot x$ and $C_{KDE} \cdot x^2$ are non-decreasing for non-negative x . We can therefore substitute the upper bound $\Delta_{perturb}$ for the distance $d_{MMD}|\theta(G, \tilde{G})$ in the inequality from Theorem E.4:

$$|\hat{f}_{KDE}(G) - \hat{f}_{KDE}(\tilde{G})| \leq L_{KDE} \cdot \Delta_{perturb} + C_{KDE} \cdot \Delta_{perturb}^2 + o(\Delta_{perturb}^2) = O(h_{min}^{-1} \Delta_{perturb} + h_{min}^{-3} \Delta_{perturb}^2)$$

This directly leads to the statement in Corollary E.6, providing theoretical backing for the objective function (Eq. (9) in the main paper), which relies on the density difference being well-behaved under controlled perturbations quantified by $\Delta_{perturb}$. \square

E.5 Derivation for Theorem E.7 (Computational Complexity)

Theorem E.7 (Computational Complexity). *The computational complexity for embedding a graph is dominated by the GNN ($O(L(md_{hid} + nd_{hid}^2))$), and computing pairwise MMD using the quadratic estimator takes $O(Sn^2 d_{out})$. Inference involves N MMD computations. Training complexity depends on batch size and MMD computations for the loss. (See Appendix E.5).*

Proof. We have total S different $k_{\gamma}^{\text{emb}} \in \mathcal{K}_{\text{emb}}$ with different hyperparameters $\Gamma_{\text{emb}} = \{\gamma_s\}_{s=1}^S$. Let $n \leftarrow n_{max}$, $m \leftarrow m_{max}$ stand for the maximum node and edge numbers of a graph. $d \approx d_{hid} \approx d_{out}$ (Usually $d_{hid} \gg d_{out}$ in practice GNNs design, so we use the worst-case as condition).

- **GNN Embedding:** $O(L(md + nd^2))$ per graph.
- **Pairwise MMD (Quadratic):** $O(Sn^2 d)$ per pair.
- **KDE Inference:** N MMDs = $O(NSn^2 d)$. Kernel evals $O(NM)$. Total $O(NSn^2 d)$.
- **Training Epoch** (Batch B , N_{pert} perturbations):
 - GNN Forward: $O(BN_{pert}L(md + nd^2))$
 - Loss MMDs (Batch ref): $O(B^2 N_{pert} Sn^2 d)$
 - Backpropagation: $O(BN_{pert}L(md + nd^2))$

Dominated by GNN passes or MMD calcs depending on relative sizes of B, N_{pert}, L, n, S . \square

E.6 Proof for Theorem E.8 (Sample Complexity)

Theorem E.8 (Sample Complexity). *To achieve L_{∞} accuracy ϵ with probability $1 - \delta$, the required number of samples N scales roughly as $N = \Omega(\epsilon^{-(2+d_{int}/\beta)})$, where β is the smoothness order of f^* and d_{int} is the intrinsic dimension. (See Appendix E.6).*

Proof. Bound L_{∞} error $\|\hat{f}_{KDE} - f^*\|_{\infty} \leq \|\hat{f}_{KDE} - \mathbb{E}\hat{f}_{KDE}\|_{\infty} + \|\mathbb{E}\hat{f}_{KDE} - f^*\|_{\infty}$.

- Bias: $O(h^{\beta})$ assuming smoothness β .
- Stochastic term: Use Lemma E.18. $\|\hat{f}_{KDE} - \mathbb{E}\hat{f}_{KDE}\|_{\infty} = O(\mathbb{E}[\hat{\mathcal{R}}_N(\mathcal{F})] + M\sqrt{\log(1/\delta)/N})$. The Rademacher complexity $\mathbb{E}[\hat{\mathcal{R}}_N(\mathcal{F})]$ for KDE class \mathcal{F} scales roughly as $O(\sqrt{1/(Nh^{d_{int}})})$ ignoring log factors. So, stochastic term is $O(\sqrt{1/(Nh^{d_{int}})} + \sqrt{\log(1/\delta)/N})$.

Now, we can set total error $\leq \epsilon$, set bias $h^\beta \sim \epsilon \implies h \sim \epsilon^{1/\beta}$, and set stochastic term $\sqrt{1/(Nh^{d_{\text{int}}})} \sim \epsilon \implies Nh^{d_{\text{int}}} \gtrsim 1/\epsilon^2$.

Substitute $h: N\epsilon^{d_{\text{int}}/\beta} \gtrsim 1/\epsilon^2 \implies N \gtrsim \epsilon^{-(2+d_{\text{int}}/\beta)}$. Combining with the $\log(1/\delta)$ term:

$$N = \Omega(\epsilon^{-(2+d_{\text{int}}/\beta)} + \frac{\log(1/\delta)}{\epsilon^2}).$$

Typically, the first term dominates for small ϵ . For $\beta = 2$ as in our Assumption 4.1 and $d_{\text{int}} = 1$, $N = \Omega(\epsilon^{-\frac{5}{2}} + \frac{\log(1/\delta)}{\epsilon^2}) = \Omega\left(\frac{1+\epsilon^{\frac{1}{2}}\log(1/\delta)}{\epsilon^{\frac{3}{2}}}\right)$. \square

E.7 Auxiliary Lemmas with Proof

This section provides detailed statements and proofs for key lemmas and remarks used in the main analysis, particularly for the robustness results in Appendix E.4.2. Several proofs are adapted and inspired from the Deep MMD-GK model [Sun and Fan, 2024], GNN properties [Hamilton *et al.*, 2017], nonparametric statistics [Wasserman, 2006] and high-dimensional statistics [Wainwright, 2019], and graph theory [Bondy *et al.*, 1976].

Remark E.9 (Interpretation of Condition E.2). *Condition E.2 imposes two complementary regularity requirements on the unknown graph-level density f^* :*

- **Boundedness.** The constraint $\|f^*\|_\infty \leq M < \infty$ rules out singularities and heavy tails, guaranteeing that all moments of interest exist and that a kernel density estimator (KDE) can achieve uniform convergence over the graph manifold \mathcal{M} .
- **f^* is bounded and has bounded second derivatives ($\beta = 2$ smoothness) on the MMD-induced Riemannian manifold.** Let the learned MMD metric be

$$d^*(G_1, G_2) = \|\mu_{P_{G_1}} - \mu_{P_{G_2}}\|_{\mathcal{H}}, \quad \mu_{P_G} = \mathbb{E}_{X \sim P_G} k(X, \cdot) \in \mathcal{H},$$

where k is a universal kernel and \mathcal{H} its RKHS. Pulling back the Euclidean metric of \mathcal{H} through the map $G \mapsto \mu_{P_G}$ endows the graph space with a Riemannian metric tensor $g_{ij}(G) = \langle \partial_{u_i} \mu_{P_G}, \partial_{u_j} \mu_{P_G} \rangle_{\mathcal{H}}$, written in local coordinates $(u_1, \dots, u_{d_{\text{int}}})$. The corresponding Laplace–Beltrami operator is

$$(\Delta_{d^*} f)(G) = \frac{1}{\sqrt{|g(G)|}} \sum_{i,j=1}^{d_{\text{int}}} \partial_{u_i} (\sqrt{|g(G)|} g^{ij}(G) \partial_{u_j} f(G)), \quad (28)$$

where g^{ij} is the inverse metric and $|g(G)| = \det[g_{ij}(G)]$. Requiring $\|\Delta_{d^*} f^*\|_\infty \leq C_\Delta$ means that f^* possesses bounded second-order derivatives along the learned geometry, i.e. it lies in the Sobolev space $W^{2,\infty}(\mathcal{M}, g)$. When the embedding degenerates to the Euclidean case $d^*(G_1, G_2) = \|\psi(G_1) - \psi(G_2)\|_2$, we have $g_{ij} = \delta_{ij}$ and (28) reduces to the classical Euclidean Laplacian $\Delta f^* = \sum_{i=1}^{d_{\text{int}}} \partial_{\psi_i}^2 f^*$, recovering the usual KDE assumption of bounded second derivatives.

- For G' inside a normal neighbourhood of G , the inverse exponential map $\text{expmap}_G^{-1}(G') = d\Phi_G^\dagger(\mu_{P_{G'}} - \mu_{P_G})$, where $d\Phi_G : T_G \mathcal{M} \rightarrow T_{\mu_{P_G}} \mathcal{H}$ is the differential of Φ and $d\Phi_G^\dagger$ is its Moore–Penrose pseudoinverse; this corresponds to projecting the difference of mean embeddings back to the tangent space at G .
- Together with the boundedness in (i), this ensures an $O(h^2)$ bias for LGKDE and yields the optimal mean-integrated squared error rate $O(n^{-4/(4+d_{\text{int}})})$ under standard kernels, as proofed in Theorem 4.3.

Lemma E.10 (Lipschitz Property of KDE Kernel). *Let $K_{\text{KDE}}(d, h)$ be the KDE kernel with bandwidth h . Define $L_K(h)$ as the Lipschitz constant of K_{KDE} with respect to the distance parameter d , satisfying:*

$$|K_{\text{KDE}}(d_1, h) - K_{\text{KDE}}(d_2, h)| \leq L_K(h)|d_1 - d_2| \quad (29)$$

For a Gaussian KDE kernel, $L_K(h) = O(1/h^{d_{\text{int}}+1})$. Then, for any distances d_{1m} and d_{2m} :

$$|K_{\text{KDE}}(d_{1m}, h) - K_{\text{KDE}}(d_{2m}, h)| \leq L_K(h)|d_{1m} - d_{2m}| \quad (30)$$

Lemma E.11 (Bound on Propagated Norms). *Under Condition E.1, let $\mathbf{Z}^{(0)} = \mathbf{X}$ with $\|\mathbf{X}\|_F \leq B_X$. Assume the normalized adjacency matrix satisfies $\|\hat{\mathbf{A}}\|_2 \leq 1$. Then the norm of the embeddings at layer l is bounded:*

$$\|\mathbf{Z}^{(l)}\|_F \leq (\rho_\sigma B_W)^l B_X \quad (31)$$

Proof. By induction. Base case $l = 0$ holds. Assume $\|\mathbf{Z}^{(l-1)}\|_F \leq (\rho_\sigma B_W)^{l-1} B_X$.

$$\begin{aligned}
\|\mathbf{Z}^{(l)}\|_F &= \|\sigma(\hat{\mathbf{A}}\mathbf{Z}^{(l-1)}\mathbf{W}^{(l)})\|_F \\
&\leq \rho_\sigma \|\hat{\mathbf{A}}\mathbf{Z}^{(l-1)}\mathbf{W}^{(l)}\|_F \quad (\text{Lipschitz } \sigma) \\
&\leq \rho_\sigma \|\hat{\mathbf{A}}\|_2 \|\mathbf{Z}^{(l-1)}\|_F \|\mathbf{W}^{(l)}\|_2 \quad (\text{Submultiplicativity}) \\
&\leq \rho_\sigma \cdot 1 \cdot \|\mathbf{Z}^{(l-1)}\|_F \cdot B_W \quad (\text{Assumptions}) \\
&\leq (\rho_\sigma B_W)((\rho_\sigma B_W)^{l-1} B_X) = (\rho_\sigma B_W)^l B_X
\end{aligned}$$

□

Lemma E.12 (Bound on Embedding Perturbation). *Let $G = (\mathbf{A}, \mathbf{X})$ and $\tilde{G} = (\tilde{\mathbf{A}}, \tilde{\mathbf{X}})$ have the same size n . Let $\|\Delta\mathbf{X}\|_F \leq B_{\Delta X}$ and $\|\hat{\tilde{\mathbf{A}}} - \hat{\mathbf{A}}\|_F \leq B_{\Delta \hat{A}}$. Under Condition E.1, the difference in final embeddings $\Delta\mathbf{Z}^{(L)} = \Phi_{\boldsymbol{\theta}}(\tilde{G}) - \Phi_{\boldsymbol{\theta}}(G)$ is bounded by:*

$$\|\Delta\mathbf{Z}^{(L)}\|_F \leq (\rho_\sigma B_W)^L B_{\Delta X} + B_{\Delta \hat{A}} \sum_{l=0}^{L-1} (\rho_\sigma B_W)^{L-l} B_{Z^{(l)}} \quad (32)$$

where $B_{Z^{(l)}} = (\rho_\sigma B_W)^l B_X$ is a bound on $\|\mathbf{Z}^{(l)}\|_F$.

Proof. From the recursive bound derived in Appendix E.4.2:

$$\|\Delta\mathbf{Z}^{(l+1)}\|_F \leq (\rho_\sigma B_W) \|\Delta\mathbf{Z}^{(l)}\|_F + (\rho_\sigma B_W \|\mathbf{Z}^{(l)}\|_2) \|\hat{\tilde{\mathbf{A}}} - \hat{\mathbf{A}}\|_F$$

Using $\|\mathbf{Z}^{(l)}\|_2 \leq \|\mathbf{Z}^{(l)}\|_F \leq B_{Z^{(l)}}$ and $\|\hat{\tilde{\mathbf{A}}} - \hat{\mathbf{A}}\|_F \leq B_{\Delta \hat{A}}$:

$$\|\Delta\mathbf{Z}^{(l+1)}\|_F \leq (\rho_\sigma B_W) \|\Delta\mathbf{Z}^{(l)}\|_F + (\rho_\sigma B_W B_{Z^{(l)}}) B_{\Delta \hat{A}}$$

Let $C_1 = \rho_\sigma B_W$. Unrolling the recursion from $l = 0$ to $L - 1$:

$$\begin{aligned}
\|\Delta\mathbf{Z}^{(L)}\|_F &\leq C_1 \|\Delta\mathbf{Z}^{(L-1)}\|_F + (C_1 B_{Z^{(L-1)}}) B_{\Delta \hat{A}} \\
&\leq C_1 (C_1 \|\Delta\mathbf{Z}^{(L-2)}\|_F + (C_1 B_{Z^{(L-2)}}) B_{\Delta \hat{A}}) + (C_1 B_{Z^{(L-1)}}) B_{\Delta \hat{A}} \\
&= C_1^2 \|\Delta\mathbf{Z}^{(L-2)}\|_F + (C_1^2 B_{Z^{(L-2)}} + C_1 B_{Z^{(L-1)}}) B_{\Delta \hat{A}} \\
&\quad \dots \\
&\leq C_1^L \|\Delta\mathbf{Z}^{(0)}\|_F + B_{\Delta \hat{A}} \sum_{l=0}^{L-1} C_1^{L-l} B_{Z^{(l)}} \\
&= (\rho_\sigma B_W)^L \|\Delta\mathbf{X}\|_F + B_{\Delta \hat{A}} \sum_{l=0}^{L-1} (\rho_\sigma B_W)^{L-l} (\rho_\sigma B_W)^l B_X \\
&= (\rho_\sigma B_W)^L \|\Delta\mathbf{X}\|_F + B_{\Delta \hat{A}} L (\rho_\sigma B_W)^L B_X
\end{aligned}$$

This provides an explicit bound $\Delta_Z = (\rho_\sigma B_W)^L (B_{\Delta X} + L B_X B_{\Delta \hat{A}})$. □

Lemma E.13 (Bound on Pairwise Distances). *Under Condition E.1, let $\mathbf{z}_u^{(l)}$ and $\mathbf{z}_v^{(l)}$ be the embeddings of nodes u, v at layer l . Assume $\|\mathbf{X}\|_F \leq B_X$. Then the Euclidean distance between node embeddings is bounded:*

$$\|\mathbf{z}_u^{(l)} - \mathbf{z}_v^{(l)}\|_2 \leq 2(\rho_\sigma B_W)^l B_X \quad (33)$$

Let $\epsilon_l = 2(\rho_\sigma B_W)^l B_X$, representing this upper bound. Then $\|\mathbf{z}_u^{(l)} - \mathbf{z}_v^{(l)}\|_2 \leq \epsilon_l$ for any pair of nodes u, v .

Proof. Follows directly from the definition of the Frobenius norm and Lemma E.11. $\|\mathbf{Z}^{(l)}\|_F^2 = \sum_{v=1}^n \|\mathbf{z}_v^{(l)}\|_2^2$. Thus $\|\mathbf{z}_v^{(l)}\|_2 \leq \|\mathbf{Z}^{(l)}\|_F$. So, $\|\mathbf{z}_u^{(l)} - \mathbf{z}_v^{(l)}\|_2 \leq \|\mathbf{z}_u^{(l)}\|_2 + \|\mathbf{z}_v^{(l)}\|_2 \leq 2\|\mathbf{Z}^{(l)}\|_F \leq 2(\rho_\sigma B_W)^l B_X$. □

Lemma E.14 (Exponential Inequality). *For any $x \in \mathbb{R}$, $|e^x - 1 - x| \leq \frac{x^2}{2} e^{|x|}$. For $x \leq 0$, $e^x \leq 1 + x + \frac{x^2}{2}$.*

Proof. The first inequality is from Taylor's theorem with remainder. $e^x = 1 + x + \frac{x^2}{2}e^c$ for some c between 0 and x . Thus $|e^x - 1 - x| = |\frac{x^2}{2}e^c| \leq \frac{x^2}{2}e^{|x|}$. For the second inequality ($x \leq 0$), consider $f(x) = 1 + x + x^2/2 - e^x$. $f(0) = 0$. $f'(x) = 1 + x - e^x$. $f'(0) = 0$. $f''(x) = 1 - e^x$. For $x < 0$, $e^x < 1$, so $f''(x) > 0$. This means $f'(x)$ increases to $f'(0) = 0$, so $f'(x) < 0$ for $x < 0$. This means $f(x)$ decreases from $f(-\infty) = \infty$ to $f(0) = 0$. Thus $f(x) \geq 0$ for $x \leq 0$. \square

Lemma E.15 (Bound on Kernel Difference). *Let $k(\mathbf{x}, \mathbf{y}) = \exp(-\|\mathbf{x} - \mathbf{y}\|^2/(2h^2))$ be the Gaussian kernel. Let $\mathbf{z}_u, \mathbf{z}_v, \tilde{\mathbf{z}}_u, \tilde{\mathbf{z}}_v$ be as defined before, with $\|\Delta \mathbf{z}_w\|_2 \leq \delta_z$ and $\|\mathbf{z}_u - \mathbf{z}_v\|_2 \leq \epsilon_{\text{bound}}$. Then:*

$$|\Delta k(u, v)| = |k(\tilde{\mathbf{z}}_u, \tilde{\mathbf{z}}_v) - k(\mathbf{z}_u, \mathbf{z}_v)| \leq \frac{\sqrt{2}}{h\sqrt{e}} \left\| \begin{pmatrix} \Delta \mathbf{z}_u \\ \Delta \mathbf{z}_v \end{pmatrix} \right\|_2 + O(\delta_z^2) \approx O(\delta_z/h) \quad (34)$$

More precisely, using and adapting the bound from MMD-GK [Sun and Fan, 2024] Lemma 3 derivation:

$$|\Delta k(u, v)| \leq \frac{2\delta_z^2 + 2\epsilon_{\text{bound}}\delta_z}{h^2} \quad (35)$$

where δ_z bounds the perturbation magnitude in node embeddings and ϵ_{bound} bounds the distance between original node embeddings.

Proof. Let $\mathbf{p} = (\mathbf{z}_u, \mathbf{z}_v)$ and $\tilde{\mathbf{p}} = (\tilde{\mathbf{z}}_u, \tilde{\mathbf{z}}_v)$ be points in $\mathbb{R}^{2d_{\text{out}}}$. Let $f(\mathbf{p}) = k(\mathbf{z}_u, \mathbf{z}_v) = \exp(-\|\mathbf{z}_u - \mathbf{z}_v\|^2/(2h^2))$. We want to bound $|f(\tilde{\mathbf{p}}) - f(\mathbf{p})|$. The gradient of f w.r.t \mathbf{p} is $\nabla f(\mathbf{p}) = \begin{pmatrix} \nabla_{\mathbf{z}_u} f \\ \nabla_{\mathbf{z}_v} f \end{pmatrix}$.

We can get that $\nabla_{\mathbf{z}_u} k(\mathbf{z}_u, \mathbf{z}_v) = -\frac{\mathbf{z}_u - \mathbf{z}_v}{h^2} k(\mathbf{z}_u, \mathbf{z}_v)$ and $\|\nabla_{\mathbf{z}_u} k(\mathbf{z}_u, \mathbf{z}_v)\|_2 = \frac{\|\mathbf{z}_u - \mathbf{z}_v\|_2}{h^2} k(\mathbf{z}_u, \mathbf{z}_v)$.

Let $t = \|\mathbf{z}_u - \mathbf{z}_v\|_2$. The norm is $\frac{t}{h^2} e^{-t^2/(2h^2)}$. This function $g(t) = te^{-t^2/(2h^2)}$ has maximum value h/\sqrt{e} at $t = h$.

So $\|\nabla_{\mathbf{z}_u} k\|_2 \leq \frac{1}{h\sqrt{e}}$. Similarly $\|\nabla_{\mathbf{z}_v} k\|_2 \leq \frac{1}{h\sqrt{e}}$.

Thus,

$$\|\nabla f(\mathbf{p})\|_2 = \sqrt{\|\nabla_{\mathbf{z}_u} k\|^2 + \|\nabla_{\mathbf{z}_v} k\|^2} \leq \sqrt{2/(h^2 e)} = \frac{\sqrt{2}}{h\sqrt{e}}.$$

By the Mean Value Theorem, $|f(\tilde{\mathbf{p}}) - f(\mathbf{p})| \leq \sup \|\nabla f\| \|\tilde{\mathbf{p}} - \mathbf{p}\|_2$.

$$\|\tilde{\mathbf{p}} - \mathbf{p}\|_2 = \sqrt{\|\tilde{\mathbf{z}}_u - \mathbf{z}_u\|^2 + \|\tilde{\mathbf{z}}_v - \mathbf{z}_v\|^2} = \sqrt{\|\Delta \mathbf{z}_u\|^2 + \|\Delta \mathbf{z}_v\|^2} \leq \sqrt{2\delta_z^2} = \sqrt{2}\delta_z.$$

So,

$$|\Delta k(u, v)| \leq \frac{\sqrt{2}}{h\sqrt{e}} (\sqrt{2}\delta_z) = \frac{2\delta_z}{h\sqrt{e}} = O(\delta_z/h).$$

For the proof of the second bound (35): Use $|e^a - e^b| \leq |a - b|$ for $a, b \leq 0$.

Let $a = -\|\tilde{\mathbf{z}}_u - \tilde{\mathbf{z}}_v\|^2/(2h^2)$ and $b = -\|\mathbf{z}_u - \mathbf{z}_v\|^2/(2h^2)$. We can get,

$$|\Delta k(u, v)| \leq |a - b| = \frac{|\|\tilde{\mathbf{z}}_u - \tilde{\mathbf{z}}_v\|^2 - \|\mathbf{z}_u - \mathbf{z}_v\|^2|}{2h^2} = \frac{|\Sigma_{uv}|}{2h^2}.$$

$$|\Sigma_{uv}| = |\|\Delta \mathbf{z}_u - \Delta \mathbf{z}_v\|^2 + 2\langle \mathbf{z}_u - \mathbf{z}_v, \Delta \mathbf{z}_u - \Delta \mathbf{z}_v \rangle| \leq 4\delta_z^2 + 4\epsilon_{\text{bound}}\delta_z.$$

Now we get that,

$$|\Delta k(u, v)| \leq \frac{4\delta_z^2 + 4\epsilon_{\text{bound}}\delta_z}{2h^2} = \frac{2\delta_z^2 + 2\epsilon_{\text{bound}}\delta_z}{h^2}.$$

This second bound might be looser if ϵ_{bound} is large, but captures the quadratic dependence on δ_z . \square

Lemma E.16 (Bound on $\|\hat{\mathbf{A}} - \hat{\mathbf{A}}\|_F$). *Let $\mathbf{A} \in \mathbb{R}^{n \times n}$ be an adjacency matrix, and $\mathbf{A}_I = \mathbf{A} + \mathbf{I}$, $d_i^{(+)} = \sum_j A_{ij} + 1$, $\mathbf{D} = \text{diag}(d_i^{(+)})$, $\hat{\mathbf{A}} = \mathbf{D}^{-1/2} \mathbf{A}_I \mathbf{D}^{-1/2}$. Let $\tilde{\mathbf{A}} = \mathbf{A} + \Delta \mathbf{A}$ be a perturbed adjacency satisfying $\|\Delta \mathbf{A}\|_{1 \rightarrow 1} < \min_i d_i^{(+)}$, and let $\tilde{\mathbf{A}}_I = \tilde{\mathbf{A}} + \mathbf{I}$, $\tilde{d}_i^{(+)} = \sum_j \tilde{A}_{ij} + 1$, $\tilde{\mathbf{D}} = \text{diag}(\tilde{d}_i^{(+)})$, $\hat{\tilde{\mathbf{A}}} = \tilde{\mathbf{D}}^{-1/2} \tilde{\mathbf{A}}_I \tilde{\mathbf{D}}^{-1/2}$. Let $d_{\min} = \min_i \{d_i^{(+)}, \tilde{d}_i^{(+)}\} > 0$ which is the smallest “augmented” degree across both original and perturbed graphs, ensuring all diagonal entries of \mathbf{D} and $\tilde{\mathbf{D}}$ are at least d_{\min} . Then*

$$\|\hat{\tilde{\mathbf{A}}} - \hat{\mathbf{A}}\|_F \leq B_{\Delta \hat{\mathbf{A}}} = O\left(n^{3/2} d_{\min}^{-2} \|\Delta \mathbf{A}\|_F\right)$$

With p_{pert} fraction of singular values be modified by factor r or $1/r$ in our proposed energy-based spectral perturbation, $\|\Delta \mathbf{A}\|_F = \|\tilde{\Sigma} - \Sigma\|_F \leq \sqrt{p_{\text{pert}} n} \cdot \sigma_{\max} \cdot \max(|r - 1|, |1/r - 1|) = B_{\Delta \mathbf{A}}$. We get

$$\|\hat{\tilde{\mathbf{A}}} - \hat{\mathbf{A}}\|_F \leq B_{\Delta \hat{\mathbf{A}}} = O\left(n^{3/2} d_{\min}^{-2} B_{\Delta \mathbf{A}}\right)$$

Proof. Let

$$\hat{\tilde{\mathbf{A}}} - \hat{\mathbf{A}} = \tilde{\mathbf{D}}^{-1/2} \tilde{\mathbf{A}}_I \tilde{\mathbf{D}}^{-1/2} - \mathbf{D}^{-1/2} \mathbf{A}_I \mathbf{D}^{-1/2},$$

and insert cross-terms to obtain

$$\hat{\tilde{\mathbf{A}}} - \hat{\mathbf{A}} = (\tilde{\mathbf{D}}^{-1/2} - \mathbf{D}^{-1/2}) \tilde{\mathbf{A}}_I \tilde{\mathbf{D}}^{-1/2} + \mathbf{D}^{-1/2} (\tilde{\mathbf{A}}_I - \mathbf{A}_I) \tilde{\mathbf{D}}^{-1/2} + \mathbf{D}^{-1/2} \mathbf{A}_I (\tilde{\mathbf{D}}^{-1/2} - \mathbf{D}^{-1/2}).$$

Taking Frobenius norms and using $\|XY\|_F \leq \|X\|_F \|Y\|_2$ gives

$$\begin{aligned} \|\hat{\tilde{\mathbf{A}}} - \hat{\mathbf{A}}\|_F &\leq \|\Delta \mathbf{D}^{-1/2}\|_F \|\tilde{\mathbf{A}}_I\|_2 \|\tilde{\mathbf{D}}^{-1/2}\|_2 \\ &\quad + \|\mathbf{D}^{-1/2}\|_2 \|\Delta \mathbf{A}\|_F \|\tilde{\mathbf{D}}^{-1/2}\|_2 \\ &\quad + \|\mathbf{D}^{-1/2}\|_2 \|\mathbf{A}_I\|_2 \|\Delta \mathbf{D}^{-1/2}\|_F, \end{aligned} \tag{36}$$

where $\Delta \mathbf{D}^{-1/2} = \tilde{\mathbf{D}}^{-1/2} - \mathbf{D}^{-1/2}$.

(i) Eigenvalue lower bound & inverse-sqrt Lipschitz. Since all diagonal entries of \mathbf{D} and $\tilde{\mathbf{D}}$ are at least d_{\min} , so $\lambda_{\min}(\mathbf{D}), \lambda_{\min}(\tilde{\mathbf{D}}) \geq d_{\min} > 0$. Utilizing the matrix-Lipschitz property of the inverse square root [Higham, 2008], the matrix function Lipschitz bound yields

$$\|\Delta \mathbf{D}^{-1/2}\|_F \leq \frac{\sqrt{n} \|\Delta \mathbf{D}\|_2}{2 d_{\min}^{3/2}} \leq \frac{\sqrt{n} n \|\Delta \mathbf{A}\|_F}{2 d_{\min}^{3/2}} = O\left(n^{3/2} d_{\min}^{-3/2} \|\Delta \mathbf{A}\|_F\right).$$

(ii) Operator-norm bounds. By construction,

$$\|\mathbf{D}^{-1/2}\|_2, \|\tilde{\mathbf{D}}^{-1/2}\|_2 \leq d_{\min}^{-1/2}, \|\mathbf{A}_I\|_2, \|\tilde{\mathbf{A}}_I\|_2 = O(1).$$

(iii) Combine. Plugging these into (36), each of the three terms is

$$O\left(n^{3/2} d_{\min}^{-2} \|\Delta \mathbf{A}\|_F\right),$$

up to constants depending on $\|\mathbf{A}_I\|_2$ and $\|\tilde{\mathbf{A}}_I\|_2$. For our proposed energy-based spectral perturbation, let p_{pert} fraction of singular values be modified by factor r or $1/r$ in, $\|\Delta \mathbf{A}\|_F = \|\tilde{\Sigma} - \Sigma\|_F \leq \sqrt{p_{\text{pert}} n} \cdot \sigma_{\max} \cdot \max(|r - 1|, |1/r - 1|) = B_{\Delta \mathbf{A}}$. We get

$$\|\hat{\tilde{\mathbf{A}}} - \hat{\mathbf{A}}\|_F \leq B_{\Delta \hat{\mathbf{A}}} = O\left(n^{3/2} d_{\min}^{-2} B_{\Delta \mathbf{A}}\right)$$

This completes the proof. \square

Lemma E.17 (MMD Stability). *Let $P_{\mathbf{Z}} = \frac{1}{n} \sum \delta_{\mathbf{z}_v}$ and $P_{\tilde{\mathbf{Z}}} = \frac{1}{n} \sum \delta_{\tilde{\mathbf{z}}_v}$ be empirical distributions of node embeddings. Let $k \in \mathcal{K}_{\text{emb}}$ be a kernel and \mathcal{H}_k its RKHS. Define $L_{\mu}(k)$ as the Lipschitz constant of the kernel mean embedding map $\mathbf{z} \mapsto \mu_{\delta_{\mathbf{z}}} = k(\cdot, \mathbf{z})$ from $(\mathbb{R}^{d_{\text{out}}}, \|\cdot\|_2)$ to $(\mathcal{H}_k, \|\cdot\|_{\mathcal{H}_k})$, satisfying:*

$$\|\mu_{\delta_{\mathbf{z}}} - \mu_{\delta_{\mathbf{z}'}}\|_{\mathcal{H}_k} \leq L_{\mu}(k) \|\mathbf{z} - \mathbf{z}'\|_2 \tag{37}$$

For a Gaussian kernel with bandwidth γ , $L_{\mu}(k) = O(1/\gamma)$. Let $L_{\mu}^* = \sup_{k \in \mathcal{K}_{\text{emb}}} L_{\mu}(k)$ be the supremum of these constants across all kernels in the family. Then:

$$d_k(P_{\mathbf{Z}}, P_{\tilde{\mathbf{Z}}}) = \|\mu_{P_{\mathbf{Z}}} - \mu_{P_{\tilde{\mathbf{Z}}}}\|_{\mathcal{H}_k} \leq L_{\mu}(k) W_1(P_{\mathbf{Z}}, P_{\tilde{\mathbf{Z}}}) \leq L_{\mu}(k) \frac{\|\Delta \mathbf{Z}\|_F}{\sqrt{n}} \tag{38}$$

where W_1 is the 1-Wasserstein distance.

Proof. The mean embedding is linear: $\mu_{P_{\mathbf{Z}}} = \frac{1}{n} \sum_v \mu_{\delta_{\mathbf{z}_v}}$.

$$\|\mu_{P_{\mathbf{Z}}} - \mu_{P_{\tilde{\mathbf{Z}}}}\|_{\mathcal{H}_k} = \left\| \frac{1}{n} \sum_v (\mu_{\delta_{\mathbf{z}_v}} - \mu_{\delta_{\tilde{\mathbf{z}}_v}}) \right\|_{\mathcal{H}_k} \leq \frac{1}{n} \sum_v \|\mu_{\delta_{\mathbf{z}_v}} - \mu_{\delta_{\tilde{\mathbf{z}}_v}}\|_{\mathcal{H}_k}.$$

By the Lipschitz assumption on the embedding map $\mathbf{z} \mapsto \mu_{\delta_{\mathbf{z}}}$:

$$\|\mu_{\delta_{\mathbf{z}_v}} - \mu_{\delta_{\tilde{\mathbf{z}}_v}}\|_{\mathcal{H}_k} \leq L_{\mu}(k) \|\mathbf{z}_v - \tilde{\mathbf{z}}_v\|_2.$$

So,

$$\|\mu_{P_{\mathbf{Z}}} - \mu_{P_{\tilde{\mathbf{Z}}}}\|_{\mathcal{H}_k} \leq \frac{L_{\mu}(k)}{n} \sum_v \|\mathbf{z}_v - \tilde{\mathbf{z}}_v\|_2.$$

The W_1 distance between $P_{\mathbf{Z}}$ and $P_{\tilde{\mathbf{Z}}}$ is $W_1(P_{\mathbf{Z}}, P_{\tilde{\mathbf{Z}}}) = \inf_{\gamma \in \Gamma(P_{\mathbf{Z}}, P_{\tilde{\mathbf{Z}}})} \int \|\mathbf{x} - \mathbf{y}\| d\gamma(\mathbf{x}, \mathbf{y})$. A valid coupling γ pairs $\delta_{\mathbf{z}_v}$ with $\delta_{\tilde{\mathbf{z}}_v}$, giving $\int \|\mathbf{x} - \mathbf{y}\| d\gamma = \frac{1}{n} \sum_v \|\mathbf{z}_v - \tilde{\mathbf{z}}_v\|_2$. Thus $W_1(P_{\mathbf{Z}}, P_{\tilde{\mathbf{Z}}}) \leq \frac{1}{n} \sum_v \|\mathbf{z}_v - \tilde{\mathbf{z}}_v\|_2$.

Also, by Cauchy-Schwarz,

$$\frac{1}{n} \sum_v \|\mathbf{z}_v - \tilde{\mathbf{z}}_v\|_2 \leq \sqrt{\frac{1}{n} \sum_v \|\mathbf{z}_v - \tilde{\mathbf{z}}_v\|_2^2} = \frac{\|\Delta \mathbf{Z}\|_F}{\sqrt{n}}.$$

Combining these gives

$$d_k(P_{\mathbf{Z}}, P_{\tilde{\mathbf{Z}}}) \leq L_{\mu}(k) W_1(P_{\mathbf{Z}}, P_{\tilde{\mathbf{Z}}}) \leq L_{\mu}(k) \frac{\|\Delta \mathbf{Z}\|_F}{\sqrt{n}}.$$

The Lipschitz constant $L_{\mu}(k)$ for the Gaussian kernel $k(\mathbf{x}, \mathbf{y}) = e^{-\|\mathbf{x} - \mathbf{y}\|^2/2h^2}$ depends on the kernel derivative bound, roughly $L_{\mu}(k) = O(1/h)$. \square

Lemma E.18 (Concentration Inequalities). *Let \mathcal{F} be a class of functions $f : \mathcal{Z} \rightarrow [0, M]$ for some constant $M > 0$. Let Z_1, \dots, Z_N be i.i.d. samples drawn from a distribution \mathbb{P} on \mathcal{Z} . Let $P_N = \frac{1}{N} \sum_{i=1}^N \delta_{Z_i}$ be the empirical measure and $Pf = \mathbb{E}_{Z \sim \mathbb{P}}[f(Z)]$. With probability at least $1 - \delta$:*

$$\sup_{f \in \mathcal{F}} \left| \frac{1}{N} \sum_{i=1}^N f(Z_i) - \mathbb{E}f(Z) \right| \leq 2\mathbb{E}[\hat{\mathcal{R}}_N(\mathcal{F})] + M \sqrt{\frac{\log(1/\delta)}{2N}} \quad (39)$$

where $\hat{\mathcal{R}}_N(\mathcal{F}) = \mathbb{E}_{\sigma}[\sup_{f \in \mathcal{F}} \frac{1}{N} \sum_{i=1}^N \sigma_i f(Z_i)]$ is the empirical Rademacher complexity of \mathcal{F} based on the sample Z_1, \dots, Z_N , and $\sigma_1, \dots, \sigma_N$ are i.i.d. Rademacher variables (± 1 with probability $1/2$).

Furthermore, for the KDE function class $\mathcal{F}_{KDE} = \{x \mapsto K(d(x, y), h) : y \in \text{Support}(\mathbb{P})\}$ where K is a kernel with bandwidth h operating in a space with intrinsic dimension d_{int} , ignoring log factors, the expected Rademacher complexity scales as:

$$\mathbb{E}[\hat{\mathcal{R}}_N(\mathcal{F}_{KDE})] = O\left(\sqrt{\frac{1}{Nh^{d_{int}}}}\right) \quad (40)$$

Proof. The first part (39) of this Lemma is a standard result in empirical process theory; see [Wainwright, 2019] for a detailed derivation. We focus on proving the bound (40) for the Rademacher complexity of the KDE function class.

Let $\mathcal{F}_{KDE} = \{f_y(x) = K(d(x, y), h) : y \in \text{Support}(\mathbb{P})\}$ be our KDE function class, where $K(d, h) = \frac{1}{C_{d_{int}} h^{d_{int}}} K_0\left(\frac{d^2}{h^2}\right)$. For a Gaussian kernel, $K_0(t) = e^{-t/2}$ and $C_{d_{int}} = (2\pi)^{d_{int}/2}$.

Step 1: Establishing Lipschitz properties of the kernel. We first establish that each function f_y is Lipschitz with respect to the input metric d . For the Gaussian kernel:

$$\left| \frac{\partial K(d, h)}{\partial d} \right| = \left| \frac{-d}{h^2} K(d, h) \right| \leq \frac{C}{h^{d_{int}+1}} \quad (41)$$

where C is a constant. This gives a Lipschitz constant of order $O(1/h^{d_{int}+1})$.

Step 2: Relating to ϵ -covering numbers. By Dudley's entropy integral [Dudley, 2014], the Rademacher complexity can be bounded using the covering numbers of \mathcal{F}_{KDE} :

$$\mathbb{E}[\hat{\mathcal{R}}_N(\mathcal{F}_{KDE})] \leq \inf_{\alpha > 0} \left\{ 4\alpha + \frac{12}{\sqrt{N}} \int_{\alpha}^{\text{diam}(\mathcal{F}_{KDE})} \sqrt{\log \mathcal{N}(\epsilon, \mathcal{F}_{KDE}, L_2(P_N))} d\epsilon \right\} \quad (42)$$

Step 3: Bounding the covering numbers. For kernel classes in d_{int} -dimensional spaces, we can bound the covering number as follows.

Let \mathcal{Y}_δ be a minimal δ -net of the support of \mathbb{P} , where $\delta = \epsilon h^{d_{int}+1}/L$, and L is the Lipschitz constant. The cardinality of this net is bounded by:

$$|\mathcal{Y}_\delta| \leq \left(\frac{D}{\delta} \right)^{d_{int}} = \left(\frac{D \cdot L}{\epsilon h^{d_{int}+1}} \right)^{d_{int}} \quad (43)$$

where D is the diameter of the support of \mathbb{P} .

For any $y \in \text{Support}(\mathbb{P})$, there exists $y' \in \mathcal{Y}_\delta$ such that $d(y, y') \leq \delta$. By Lipschitz continuity:

$$\|f_y - f_{y'}\|_{L_2(P_N)} \leq L \cdot \delta = \epsilon \quad (44)$$

Therefore, $\{f_{y'} : y' \in \mathcal{Y}_\delta\}$ forms an ϵ -cover of \mathcal{F}_{KDE} with respect to $L_2(P_N)$, and:

$$\log \mathcal{N}(\epsilon, \mathcal{F}_{KDE}, L_2(P_N)) \leq \log |\mathcal{Y}_\delta| \leq d_{int} \log \left(\frac{D \cdot L}{\epsilon h^{d_{int}+1}} \right) \quad (45)$$

Substituting $L = O(1/h^{d_{int}+1})$:

$$\log \mathcal{N}(\epsilon, \mathcal{F}_{KDE}, L_2(P_N)) \leq d_{int} \log \left(\frac{D \cdot O(1/h^{d_{int}+1})}{\epsilon h^{d_{int}+1}} \right) = d_{int} \log \left(\frac{D \cdot O(1)}{\epsilon h^{2d_{int}+2}} \right) \quad (46)$$

Step 4: Evaluating Dudley's integral. Substituting into Dudley's integral:

$$\mathbb{E}[\hat{\mathcal{R}}_N(\mathcal{F}_{KDE})] \leq \inf_{\alpha > 0} \left\{ 4\alpha + \frac{12}{\sqrt{N}} \int_{\alpha}^M \sqrt{d_{int} \log \left(\frac{D \cdot O(1)}{\epsilon h^{2d_{int}+2}} \right)} d\epsilon \right\} \quad (47)$$

$$= \inf_{\alpha > 0} \left\{ 4\alpha + \frac{12\sqrt{d_{int}}}{\sqrt{N}} \int_{\alpha}^M \sqrt{\log \left(\frac{D \cdot O(1)}{\epsilon h^{2d_{int}+2}} \right)} d\epsilon \right\} \quad (48)$$

Using the fact that $\int_{\alpha}^M \sqrt{\log(c/\epsilon)} d\epsilon = O(M\sqrt{\log(c/\alpha)})$ for any $c > 0$, and choosing α optimally:

$$\mathbb{E}[\hat{\mathcal{R}}_N(\mathcal{F}_{KDE})] = O \left(\frac{1}{\sqrt{N}} \sqrt{d_{int} \log \left(\frac{1}{h^{2d_{int}+2}} \right)} \right) \quad (49)$$

$$= O \left(\frac{1}{\sqrt{N}} \sqrt{d_{int}(2d_{int}+2) \log \left(\frac{1}{h} \right)} \right) \quad (50)$$

Step 5: Simplification. For any fixed dimension d_{int} and ignoring logarithmic factors in h :

$$\mathbb{E}[\hat{\mathcal{R}}_N(\mathcal{F}_{KDE})] = O \left(\frac{1}{\sqrt{N}} \right) \cdot O(1) = O \left(\frac{1}{\sqrt{N}} \right) \quad (51)$$

For a more precise bound accounting for the dependence on bandwidth h , we need to consider the scaling of the kernel values themselves. The magnitude of Gaussian kernel functions scales as $O(1/h^{d_{int}})$. This introduces an additional factor of $1/h^{d_{int}/2}$ in the Rademacher complexity, resulting in:

$$\mathbb{E}[\hat{\mathcal{R}}_N(\mathcal{F}_{KDE})] = O \left(\sqrt{\frac{1}{Nh^{d_{int}}}} \right) \quad (52)$$

This matches known results in nonparametric statistics for KDE in d_{int} -dimensional spaces, as established by [Giné and Nickl, 2009]. \square

F More Experiment Details

F.1 Baseline Methods

We provide detailed descriptions of the baseline methods used in our experiments:

F.1.1 Traditional Graph Kernel Methods

- **Weisfeiler-Lehman (WL) Kernel** [Shervashidze *et al.*, 2011]: A graph kernel that iteratively aggregates and hashes node labels to capture structural information. The kernel value between two graphs is computed based on the count of identical node labels after iterations.
- **Propagation Kernel (PK)** [Neumann *et al.*, 2016]: A graph kernel that measures graph similarity through propagated node label distributions, effectively capturing both local and global graph properties.
- **Isolation Forest (IF)** [Liu *et al.*, 2008]: An anomaly detection algorithm that isolates observations by randomly selecting a feature and a split value. Anomalies require fewer splits to be isolated.
- **One-Class SVM (OCSVM)** [Amer *et al.*, 2013]: A one-class classification method that learns a decision boundary that encloses normal data points in feature space.

F.1.2 Deep Learning Methods

- **OCGIN** [Zhao and Akoglu, 2021]: Combines Graph Isomorphism Network with Deep SVDD for anomaly detection. It learns a hyperspherical decision boundary in the embedding space to separate normal from anomalous graphs.
- **GLocalKD** [Ma *et al.*, 2022]: Employs knowledge distillation to capture both global and local patterns of normal graphs. The model distills knowledge from a teacher network to a student network at both graph and node levels.
- **OCGTL** [Qiu *et al.*, 2022]: Uses neural transformation learning to address the performance flip issue in graph-level anomaly detection. It learns transformation-invariant representations through multiple graph transformations.
- **SIGNET** [Liu *et al.*, 2023b]: A self-interpretable graph anomaly detection method that simultaneously learns to detect anomalies and provide explanations through multi-view subgraph information bottleneck.
- **GLADC** [Luo *et al.*, 2022]: Utilizes graph-level adversarial contrastive learning to identify anomalies. It learns discriminative features through contrastive learning with adversarial augmentations.
- **CVTGAD** [Li *et al.*, 2023]: Employs a transformer structure with cross-view attention for graph anomaly detection. It captures both structural and attribute information through multiple views of graphs.

F.2 Evaluation Metrics

We employ three widely-used metrics to evaluate anomaly detection performance:

F.2.1 Area Under the ROC Curve (AUROC)

AUROC measures the model’s ability to distinguish between normal and anomalous graphs across different threshold settings. Given true labels y and predicted anomaly scores s , AUROC is computed as:

$$\text{AUROC} = \frac{\sum_{i \in P} \sum_{j \in N} \mathbf{1}(s_i > s_j)}{n_p n_n} \quad (53)$$

where P denotes the set of positive (anomalous) samples and N the set of negative (normal) samples. The term $\mathbf{1}(s_i > s_j)$ is an indicator function that takes the value 1 if $s_i > s_j$, and 0 otherwise. n_p and n_n are the numbers of positive and negative samples, respectively. AUROC ranges from 0 to 1, with 1 indicating perfect separation and 0.5 indicating random guessing. A higher AUROC value indicates better detection performance.

F.2.2 Area Under the Precision-Recall Curve (AUPRC)

AUPRC focuses on the trade-off between precision and recall, which is particularly important for imbalanced datasets where anomalies are rare. Given predictions at different thresholds:

$$\text{Precision} = \frac{\text{TP}}{\text{TP} + \text{FP}}, \quad \text{Recall} = \frac{\text{TP}}{\text{TP} + \text{FN}} \quad (54)$$

where TP, FP, and FN are the numbers of true positives, false positives, and false negatives, respectively. AUPRC is computed as the area under the precision-recall curve, which can be approximated using the trapezoidal rule [Atkinson and Han, 2005]:

$$\text{AUPRC} = \sum_{i=1}^n (\text{Recall}_i - \text{Recall}_{i-1}) \cdot \frac{\text{Precision}_i + \text{Precision}_{i-1}}{2} \quad (55)$$

AUPRC ranges from 0 to 1, with higher values indicating better performance. Unlike AUROC, AUPRC is more sensitive to imbalanced data distributions, making it a better metric for anomaly detection and rare event classification.

F.2.3 False Positive Rate at 95% Recall (FPR95)

FPR95 measures the false positive rate when the true positive rate (recall) is fixed at 95%. It is computed as:

$$\text{FPR95} = \frac{\text{FP}}{\text{TN} + \text{FP}} \text{ at TPR} = 0.95 \quad (56)$$

where TN represents true negatives. Lower FPR95 values indicate better performance, as they represent fewer false alarms while maintaining a high detection rate of anomalies.

This metric is particularly relevant for real-world applications where maintaining a high detection rate of anomalies is crucial, but false alarms need to be minimized. A lower FPR95 indicates that the model can achieve high recall with fewer false positives.

These three metrics together provide a comprehensive evaluation of anomaly detection performance:

- AUROC evaluates overall ranking ability
- AUPRC focuses on precision in imbalanced settings
- FPR95 assesses practical utility with fixed high recall

F.3 Implementation Details of LGKDE

We provide detailed information about our LGKDE implementation. The framework consists of three main components: graph representation learning, MMD-based metric learning, and multi-scale kernel density estimation.

F.3.1 Graph Neural Network Architecture

The GNN backbone of our model uses a Graph Isomorphism Network (GCN) architecture with the following specifications:

- L GCN layers with hidden dimension 32
- Batch normalization after each layer to enhance the stability
- Dropout rate of 0.2 for regularization
- ReLU activation function between layers

F.3.2 MMD-based Graph Distance

For computing graph distances, we employ Maximum Mean Discrepancy (MMD) with multiple bandwidths:

- We use multiple bandwidth values {0.01, 0.1, 1, 10, 100} to capture different scales of variations

The deep graph MMD computation preserves fine-grained structural information compared to graph-level pooling.

F.3.3 Training Details

The model is trained with the following specifications:

- Optimizer: Adam with a learning rate of 0.001 in default. We also employ gradient clipping and the learning rates are scheduled with a warm-up period followed by cosine decay.
- Batch size: 128 and full batch size for test datasets
- Training epochs: Maximum 500 with early stopping patience of 10. The early stopping is based on validation set performance to prevent overfitting.

F.3.4 Ablation Study Settings

For the ablation studies examining different components:

- Multi-scale KDE: Compare learnable weights versus fixed uniform weights
- Graph distance computation: Compare MMD-based distance with simpler alternatives:
 - Graph-level pooling (sum/average) followed by Euclidean distance
 - Single-scale kernel
- Graph neural architecture: Vary GNN depth and width to examine model capacity

Our implementation is based on both PyTorch Geometric [Fey and Lenssen, 2019] and DGL [Wang, 2019] frameworks.

F.4 Implementation Details of Baseline Methods and Codes

All our benchmark experiments follow the unified benchmarks for graph anomaly detection [Wang *et al.*, 2024] and are implemented on both PyTorch Geometric [Fey and Lenssen, 2019] and GraKeL [Siglidis *et al.*, 2020]. For all GNN-based methods (OCGIN, GLocalKD, OCGTL, SIGNET, GLADC, CVTGAD), we use GIN as the backbone with 3 layers and hidden dimension 32. The batch size is set to 128. For OCGIN, we use a learning rate of 0.0001. For GLocalKD, we set the output dimension to 32. For OCGTL, the learning rate is 0.001. For SIGNET, we use a learning rate of 0.0001 and a hidden dimension of 128. For GLADC, we use hidden dimension 32, dropout 0.1, and learning rate 0.001. For CVTGAD, we use random walk dimension 16, degree dimension 16, number of clusters 3, alpha 1.0, and GCN as an encoder with global mean pooling.

For graph kernel methods, WL and PK kernels are combined with iForest (200 trees, 0.5 sample ratio) and OCSVM (nu=0.1). The number of epochs for kernel methods is set to 30.

All experiments are run on NVIDIA RTX 4090 GPUs. Each method is run 5 times with different random seeds to obtain stable results. More details on the implementation can be found in our released codebase (Code will be public and open source after paper acceptance (currently under review); Here provide a main snippet of our proposed LGKDE implementation in Listing 1).

Listing 1: LGKDE Code Snippet

```
from model import DGMMMD
class LGKDE(nn.Module):
    """
    Our proposed Algorithm LGKDE
    """
```

```

    def __init__(self,
                 in_dim: int,
                 hidden_dim: int,
                 out_dim: int,
                 num_layers: int,
                 bandwidths: List[float] = [0.01, 0.1, 1.0, 10,
                                             100],
                 dropout: float = 0.2,
                 batch_norm: bool = True,
                 learn_kde_weights: bool = True):
        super().__init__()

        self.dgmmd = DGMMD(
            in_dim=in_dim,
            hidden_dim=hidden_dim,
            out_dim=out_dim,
            num_layers=num_layers,
            bandwidths=bandwidths,
            dropout=dropout,
            batch_norm=batch_norm,
        )

        # Learnable weights for multi-scale KDE
        self.kde_logits = nn.Parameter(torch.ones(len(
            bandwidths))/len(bandwidths))
        self.kde_dimension = kde_dimension

        # Optionally freeze KDE weights
        if not learn_kde_weights:
            self.kde_logits.requires_grad_(False)

    def compute_kde_scores(self, dist_matrix: torch.Tensor) \
        -> torch.Tensor:
        """
        Compute KDE scores from distance matrix using
        learned bandwidth weights.

        Args:
            dist_matrix: Shape (M, N) pairwise distances
        Returns:
            torch.Tensor: Shape (M,) KDE scores
        """
        alpha = F.softmax(self.kde_logits, dim=0)
        M, N = dist_matrix.size()

        total_kde = torch.zeros(M, device=dist_matrix.
                               device, dtype=dist_matrix.dtype)
        for k, bw in enumerate(self.dgmmd.bandwidths):
            exponent = -0.5 * (dist_matrix / bw)**2
            kernel_vals = torch.exp(exponent)
            partial_kde = (1.0 / N) * kernel_vals.sum(dim
                =1) / ((2*math.pi*(bw**2)) ** (0.5*self.
                kde_dimension))
            total_kde += alpha[k] * partial_kde

        return total_kde

    def get_reference_scores(self, reference_graphs: dgl.
                           DGLGraph) -> torch.Tensor:
        """
        Compute density scores for reference set (usually
        training graphs).
    
```

```

Args:
    reference_graphs: Batched reference graphs
Returns:
    torch.Tensor: Density scores for reference
                  graphs
"""
ref_dist = self.dgmmmd.compute_distance_matrix(
    reference_graphs, graphs_b=None)
return self.compute_kde_scores(ref_dist)

def get_query_scores(self, query_graphs: dgl.DGLGraph,
                     reference_graphs: dgl.DGLGraph) -> torch.Tensor:
    """
    Compute density scores for query graphs relative to
    reference graphs.

    Args:
        query_graphs: Batched query graphs
        reference_graphs: Batched reference graphs
    Returns:
        torch.Tensor: Density scores for query graphs
    """
    query_dist = self.dgmmmd.compute_distance_matrix(
        query_graphs, graphs_b=reference_graphs)
    return self.compute_kde_scores(query_dist)

@torch.no_grad()
def get_anomaly_scores(
    self,
    test_graphs: dgl.DGLGraph,
    train_graphs: dgl.DGLGraph,
    threshold_percentile: float = 10
):
    """
    Compute anomaly scores and threshold for test
    graphs.

    Args:
        test_graphs: Batched test graphs
        train_graphs: Batched training graphs
        threshold_percentile: Percentile for anomaly
                              threshold
    Returns:
        (test_scores, train_scores, predictions,
         threshold)
    """
    self.eval()

    # Compute scores
    train_scores = self.get_reference_scores(
        train_graphs)
    test_scores = self.get_query_scores(test_graphs,
                                        train_graphs)

    # Compute threshold from training scores
    threshold = torch.quantile(train_scores,
                               threshold_percentile/100)
    predictions = (test_scores <= threshold).int()

    return test_scores, train_scores, predictions,
           threshold

```

Limitations and Future Work

Computational Complexity. Our theoretical analysis already offers a formal analysis showing that LGKDE incurs an $O(N^2)$ time and memory footprint due to the all-pairs MMD evaluation across N graphs. While this cost is entirely manageable for the TU benchmarks used in our study (largest dataset $\leq 5,000$ graphs) and for most graph-level anomaly-detection workloads encountered in practice, we acknowledge that such quadratic scaling can become a potential bottleneck on million-graph corpora. A fruitful direction is therefore to investigate *structure-preserving accelerations*—for example, adaptive graph sparsification or low-rank kernel approximations—that reduce the effective number of pairwise comparisons yet retain the theoretical guarantees of deep MMD. Developing such techniques without compromising LGKDE’s statistical properties is left for future work.

Graph Domains and Modalities. Our experiments target undirected, homogeneous graphs with discrete node attributes. Extending LGKDE to heterogeneous (multi-relational) graphs, graphs with rich edge features (e.g., impedances in power grids), and temporal or dynamic graphs remains open. Potential Future work can investigate plug-and-play relational or temporal encoders—such as RGAT for multi-relational data and TGNNs for time-evolving structures—so that the density estimator can natively model modality-specific inductive biases.

Statement of Broader Impacts

This work introduces LGKDE, a learnable kernel density estimation framework for graphs that advances both theoretical understanding and practical capabilities in graph analysis. The method’s strong performance in graph anomaly detection demonstrates its potential impact across various domains, from identifying anomalous molecular structures in drug discovery to detecting suspicious patterns in network security. The learnable nature of our approach makes it particularly valuable for domains where traditional fixed kernels may fail to capture domain-specific patterns.

From a broader perspective, LGKDE contributes to the development of more principled and interpretable graph analysis methods, as its theoretical foundations provide clear understanding of its behavior and limitations. While the method shows promise for various beneficial applications, users should carefully consider data quality and privacy implications when applying it to sensitive datasets. To the best of our knowledge, our research does not raise explicit ethical concerns nor introduce religious or cultural constraints.